Mantle metasomatic influence on water contents in continental lithosphere: New constraints from garnet pyroxenite xenoliths (France & Cameroon volcanic provinces)

Samantha Azevedo-Vannson, Lydéric France, Jannick Ingrin, Gilles Chazot

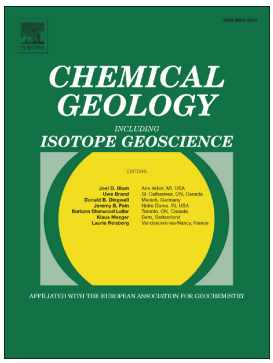

Mantle metasomatic influence on water contents in continental lithosphere: New constraints from garnet pyroxenite xenoliths (France & Cameroon volcanic provinces)

Samantha Azevedo-Vannson, Lydéric France, Jannick Ingrin, Gilles Chazot

PII: S0009-2541(21)00201-1

DOI: https://doi.org/10.1016/j.chemgeo.2021.120257

Reference: CHEMGE 120257

To appear in: *Chemical Geology*

Received date: 6 January 2021

Revised date: 7 April 2021

Accepted date: 14 April 2021

Please cite this article as: S. Azevedo-Vannson, L. France, J. Ingrin, et al., Mantle metasomatic influence on water contents in continental lithosphere: New constraints from garnet pyroxenite xenoliths (France & Cameroon volcanic provinces), *Chemical Geology* (2021), https://doi.org/10.1016/j.chemgeo.2021.120257

Mantle metasomatic influence on water contents in continental lithosphere: new constraints from garnet pyroxenite xenoliths (France & Cameroon volcanic provinces)

Samantha Azevedo-Vannson[1,2,*] samantha.azevedo-vannson@mnhn.fr**; Lydéric France[1]; Jannick Ingrin[3]; Gilles Chazot[4]**

[1]Université de Lorraine, CNRS, CRPG, F-54000 Nancy, France

[2]Muséum National d'Histoire Naturelle, Institut de Minéralogie, de Physique des Matériaux, et de Cosmochimie (IMPMC), UMR CNRS 7590, Sorbonne Université, 61 rue Buffon, F-75005 Paris, France

[3]Univ. Lille, CNRS, INRAE, ENSCL, UMR 8207 - UMET - Unité Matériaux et Transformations, F-59000 Lille, France

[4]Univ. Brest, CNRS, IUEM, UMR 6538, Laboratoire Géosciences Ocean, Place Copernic, 29280 Plouzané, France

[*]Corresponding author.

Abstract

Quantifying water contents in the lithospheric mantle is key to our understanding of global geodynamics, mantle composition, and related physical properties. Most mantle lithologies (peridotite) contain little water (~50 ppm), but petrological heterogeneities such as pyroxenites are more hydrous (~300 ppm) relative to the mantle rocks. Pyroxenites also melt at lower temperatures than peridotites and are thus important to magma genesis. Thus, quantifying pyroxenite water contents provides new information on the distribution of water in the mantle. Here, we present phase-specific FTIR measurements of the water contents in pyroxenite mantle xenoliths from two continental lithospheric domains that experienced intense metasomatism: the French Massif Central (FMC, France) and the Adamawa Volcanic Plateau (AVP, Cameroon). The AVP garnet pyroxenites are more hydrated ($[H_2O]_{Clinopyroxene}$ = 386–685 ppm; $[H_2O]_{Orthopyroxene}$ = 124–155 ppm; $[H_2O]_{Garnet}$ < 0.5 ppm) than FMC ones ($[H_2O]_{Clinopyroxene}$ = 112–465 ppm; $[H_2O]_{Orthopyroxene}$ = 61–104 ppm; $[H_2O]_{Garnet}$ < 0.5 ppm). These water concentrations are homogenous at the grain and correlate with equilibrated major element concentrations, indicating that they are representative of lithospheric water, although

the FMC pyroxenites were dehydrated during metasomatism by a carbonatitic fluid (based on the correlation between La_N/Sm_N and Ti/Eu ratios); the water contents of AVP pyroxenites were likely not affected by metasomatism. FMC pyroxenites show peculiar FTIR spectra that may reflect the preferential dehydration of specific sites in the pyroxene structure. In both regions, metasomatism modified the light rare Earth element contents (e.g., Ce) of the pyroxenites, resulting in highly variable H_2O/Ce ratios. Therefore, we conclude that the utility of the H_2O/Ce ratio to identify the involvement of pyroxenites in magmas genesis is limited.

Keywords: nominally anhydrous minerals; garnet pyroxenites; hydroxyl; mantle metasomatism; Adamawa Volcanic Plateau; French Massif Central

1. Introduction

Water in the silicate Earth is mainly concentrated in the mantle, which contains a mass of water equivalent to 4–10 times that in the oceans (Marty et al., 2016; Peslier et al., 2017). Water in the mantle can be hosted in hydrous minerals such as amphiboles or micas (e.g., up to 2 wt% H_2O in amphibole: Bizimis and Peslier, 2015; Green, 2015) or as hydrogen point defects in nominally anhydrous minerals (NAMs) due to the replacement of cations in their mineral structures by hydrogen atoms (Demouchy and Bolfan-Casanova, 2016). Although NAMs do not contain free molecular H_2O, their hydrogen concentrations are generally expressed as ppm H_2O equivalent. In the upper mantle rocks (peridotites and pyroxenites), different NAMs have various storage capacities: garnet is generally anhydrous and contains little water (Rossman and Smyth, 1990; Bell and Rossman, 1992; Matsyuk et al., 1998; Beran and Libowitzky, 2006), as does olivine (up to 40 ppm H_2O; Yu et al., 2011; Doucet et al., 2014; Hui et al., 2015), whereas clinopyroxene and orthopyroxene can contain 100–400 and 50–200 ppm H_2O, respectively (Fig. 1, Table 1; Peslier et al. (2002, 2012), Peslier (2010), Xia et al. (2010, 2013), Yu et al. (2011), Hao et al. (2012, 2014, 2016a, 2016b, 2018), Doucet et al. (2014), Warren and Hauri (2014), Bizimis and Peslier (2015), Demouchy

et al. (2015), Li et al. (2015, 2018), and Peslier and Bizimis (2015), Kilgore et al. (2018, 2020), Schaffer et al. (2019), Ashley et al. (2020)).

Despite its low concentrations in the mantle, water has many effects on mantle properties: it decreases mineral electrical resistivities (Selway, 2014), olivine aggregate viscosities (Hirth and Kohlstedt, 1996), and peridotite melting temperatures (Asimow et al., 2004; Green et al., 2010; Kovács et al., 2012). Water also acts as a lubricant for plate tectonics by weakening olivine (Karato, 1990; Hirth and Kohlstedt, 1996; Fei et al., 2013; Peslier and Bizimis, 2015). Therefore, it is necessary to quantify the distribution and concentrations of water in the mantle to better understand geodynamics at the global scale.

Water is heterogeneously distributed in mantle domains. The mantle source of mid-ocean ridge basalts (MORBs), i.e., the depleted MORB mantle (DMM), contains a relatively uniform 70–160 ppm H_2O (Salters and Stracke, 2004; Workman and Hart, 2005), although these results should be considered with caution because MORBs likely represent homogenized final products. The mantle source of ocean island basalts (OIBs), i.e., the FOcal ZOne (FOZO), high-μ (HIMU), primitive mantle (PM), and enriched mantle (EM) reservoirs, is rather heterogeneous and more hydrated (96–750 ppm H_2O, depending on the specific reservoir; McDonough and Sun, 1995; Dixon and Clague, 2001; Dixon et al., 2002; Wallace, 2002; Workman et al., 2004, 2006; Cabral et al., 2014; Kendrick et al., 2014, 2015). The mantle transition zone is also likely water-rich (e.g., Bolfan Casanova et al., 2012). Therefore, water is likely present throughout the upper mantle and at different concentrations in the individual reservoirs. Variations also exist within each reservoir; for example, EM reservoirs are thought to contain between 90 and 400 ppm H_2O (Bizimis and Peslier, 2015). Because hydrogen is both volatile and incompatible, its concentration in minerals is modified by processes including partial melting, crystallization, and metasomatism. Furthermore, given the large variation of hydrogen concentrations between olivine and pyroxene, different mantle

lithologies (e.g., dunite, harzburgite, pyroxenite, etc.) likely have diverse bulk water contents (0–120 and 0–350 ppm H_2O in peridotites and pyroxenites, respectively; Fig. 1, Table 1).

The lithospheric upper mantle may contain 5% pyroxenites (Kornprobst, 1969; Pearson et al., 1993), comprising eclogites (recycled oceanic crust; Allègre and Turcotte, 1986; Viljoen et al., 2005; Gonzaga et al., 2010; Montanini et al., 2012) and high-pressure cumulates fractionated from basaltic magmas percolating through the lithospheric mantle (O'Hara and Yoder, 1967; Viljoen et al., 2005; Downes, 2007; Gonzaga et al., 2010; Perinelli et al., 2011; France et al., 2015), which have distinct geochemical signatures (e.g., O isotopic data, trace elements) from one another (e.g., Gonzaga et al., 2010; Pezzali et al., 2015). Despite the low abundance of pyroxenites in lithospheric mantle domains, their relatively high-water contents make them important lithologies for constraining the global water budget of the upper mantle. Indeed, because of their different chemical and modal compositions (<40% olivine, although some exceptions exist at high pressure; Green et al., 2010; Kovács et al., 2012; Lambart et al., 2016), the melting temperatures of most pyroxenites are lower than those of peridotites (Lambart et al., 2016). This implies that pyroxenites can contribute up to 40% of the total melt formed during basalt magma genesis (Mallick et al., 2015). In contrast, if the surrounding mantle is partially molten, the consumption of pyroxenite-derived melts is limited to less than 20% due to liquid reactivity (Lambart et al., 2012). Evidence of such heterogeneities is visible in percolated mantle domains (e.g., Borghini et al., 2016; Sanfilippo et al., 2017) and in magmas erupted at the surface in various geodynamic settings (rift related, Rooney et al., 2014; MORBs and OIBs, Sobolev et al., 2007; Shorttle et al., 2014). Furthermore, in some cases, melts derived from eclogite-bearing peridotite sources can react with the surrounding mantle to form secondary pyroxenites (Borghini et al., 2016). Hence, pyroxenites are at least as involved in magma genesis as peridotites (Hirschmann and Stolper, 1996; Lambart et al., 2009). Because the mantle sources of magmas are commonly at depths

where garnet pyroxenites are stable (deeper than 45 km), those lithologies are essential to our understanding of magma genesis. Nevertheless, few data are available on the water contents of garnet pyroxenites (Bizimis and Peslier, 2015; Hao et al., 2018; Li et al., 2018).

In this study, we present new data on the water contents of NAMs in garnet pyroxenites from two continental domains: the French Massif Central (FMC, France) and the Adamawa Volcanic Plateau (AVP, Cameroon). We use our results to constrain the contribution of garnet pyroxenites to the water distribution in the subcontinental lithospheric mantle. By comparing these water contents to trace element data, we discuss the effects of mantle metasomatism on the distribution and concentration of water in the subcontinental lithospheric mantle. Our results reveal varying degrees of metasomatic dehydration of NAMs of FMC pyroxenites and thus highly variable H_2O/Ce ratios, limiting the reliability of H_2O/Ce ratios for tracking the influence of garnet pyroxenites during magma genesis.

2. Geological settings and sample descriptions

The studied garnet pyroxenite xenoliths record some of the mineralogical and petrological heterogeneities of the continental lithospheric mantle beneath the FMC and the AVP. Petrological and geochemical characteristics (textures, bulk-rock and phase-specific major and trace element concentrations, and O-Sr-Nd isotopes), together with geodynamic interpretations of the genesis and pressure-temperature-time evolution of these samples are available in France et al. (2015). These garnet pyroxenites are mantle cumulates that crystallized from percolating melts at 1–2 GPa during post-collisional magmatism (possibly of Hercynian age in the FMC and Pan-African age in the AVP; France et al., 2015). Their textures and chemical compositions were subsequently fully re-equilibrated at various pressure-temperature conditions (France et al., 2015). Here, we briefly summarize the geological histories of these two regions.

2.1. French Massif Central

The lithospheric mantle beneath the FMC is composed of two domains north and south of ~45°30'N (Lenoir et al., 2000; Fig. 2a) inherited from the Hercynian orogeny and characterized by different petrological and geochemical properties. The northern domain is refractory, enriched in light rare-earth elements (LREEs), and similar to the cratonic subcontinental lithospheric mantle; it is thus considered to be a pre-Variscan lithospheric block. The southern domain is more juvenile and likely accreted during the Hercynian orogeny (Lenoir et al., 2000). Both domains have been enriched by metasomatic fluids. Based on REE data, Wittig et al. (2007) interpreted that the northern and southern domains were metasomatized by carbonatitic fluids and silicate melts, respectively. However, Gu et al. (2016, 2018) recently showed that the southern domain was also metasomatized by either fluid with carbonatitic affinities or melt/fluid interactions related to subducted materials.

Garnet pyroxenite xenoliths mainly comprise clinopyroxene and garnet and are from two volcanic areas in the southern domain: the Devès (Marais de Limagne and Saint-Didier d'Allier basaltic maars) and the Languedoc (Le Pouget basaltic maar) volcanic fields (France et al., 2015; Fig. 2a). In the corresponding pyroclastic deposits, most xenoliths are peridotitic, pyroxenites are less common, and garnet pyroxenites are extremely rare: only five samples have been reported in the FMC, one in Touron (2005) and four in France et al. (2015), corresponding to those studied herein. All samples from the Devès volcanic field (LN78, LP27, and SD53) show evidence of metasomatism (e.g., amphiboles in LN78), whereas that from Le Pouget has not been affected by any metasomatic process (France et al., 2015). Amphiboles in these samples are not part of the primary cumulate assemblage, but result from metasomatic interactions between the primary magmatic mineral assemblage (garnet, clinopyroxenes, orthopyroxenes, and spinel) and a metasomatic fluid (France et al., 2015).

2.2. Adamawa Volcanic Plateau

The AVP basement formed during the Eburnean orogeny 2.1 Ga and was reworked during the Pan-African orogeny and by subsequent granite intrusions ~520 Ma (Castaing et al., 1994; Fig. 2b). During the break-up of Pangea, the lithospheric mantle domain was metasomatized by a hydrous silicate melt (Lee et al., 1996; Temdjim et al., 2004; France et al., 2015; Njombie et al., 2018). The alkaline AVP is in the northern part of the Cameroon Volcanic Line, a large plutonic and volcanic province emplaced from 65 Ma to present (see chronological summary by Njome and de Wit, 2014).

Pyroxenite xenoliths (YK01, YK03, YK05, YK12, YK13, and YK16) were sampled at the Youkou basaltic maar. In the corresponding pyroclastic deposits, most xenoliths are peridotitic, and pyroxenites are less common. Pyroxenites mainly comprise clinopyroxene and garnet (Table 2). All xenoliths were metasomatized, and all samples except YK01 contain rare secondary amphiboles that result from metasomatic interactions at depth between the primary magmatic mineral assemblage (garnet, clinopyroxenes, orthopyroxenes, and spinel) and a metasomatic agent (France et al., 2015). Two groups of xenoliths have been defined based on their petrographic characteristics; the first (YK01, YK05 and YK16) contains cm-sized megacrysts of clinopyroxene with exsolved garnet crystals, whereas the second (YK03, YK12 and YK13) is composed of mm-sized granular assemblages (France et al., 2015).

3. Petrographic characterization and metasomatic interactions

3.1. Pyroxenites as metacumulates

Here, we summarize the main petrographic characteristics of the pyroxenite xenoliths to highlight that the studied samples are mantle metacumulates that suffered mantle

metasomatism. A detailed description and interpretation of the origin and evolution of these samples in their geodynamic context is available in France et al. (2015).

The FMC pyroxenites show recrystallized granoblastic textures. Samples LN78, LP27, and SD53 have average grain sizes of 1 mm, whereas the Le Pouget sample is finer grained with pyroxenes averaging 0.25 mm and spinel and garnet 0.75 mm . Based on the corresponding bulk-rock heavy REE (HREE) enrichments, garnet was likely part of the liquidus assemblage that formed the cumulates (see section 3.2 and details in France et al., 2015). Nevertheless, the garnets currently present in the samples are likely metamorphic; garnets often enclose green spinel and contain numerous spinel, plagioclase, orthopyroxene, and clinopyroxene inclusions surrounded by radial fractures (Fig. 3a). Those inclusions record the transition from the garnet-free Seiland pyroxenite facies to the garnet-bearing Ariegite pyroxenite facies under changing pressure-temperature (P-T) conditions (likely decreasing P; France et al., 2015). Several large clinopyroxene grains display orthopyroxene exsolutions (e.g., LN78, Fig. 3b), indicating an early decrease in temperature. Local assemblages of finer grained plagioclase, brown spinel, and orthopyroxene are in contact with both clinopyroxene and garnet, suggesting a late re-equilibration in the Seiland subfacies (France et al., 2015).

The AVP pyroxenites of the first petrological group (France et al., 2015) contain clinopyroxene megacrysts (0.5–3 cm) with garnet exsolutions (Fig. 3d), and additional garnet is present around spinel grains. Sample YK05 records crystal-plastic deformation (Fig. 3d) and shows additional orthopyroxene exsolutions in clinopyroxene. The second group of AVP pyroxenites comprise mm-sized granular assemblages (~3 mm) with clinopyroxenes containing exsolutions of garnet, amphibole, and spinel (Fig. 3c; France et al., 2015). Garnet is both exsolved from and bordering clinopyroxene grains. Very thin (~1–2 μm) spinel exsolutions are also present in clinopyroxenes. Exsolutions of garnet and orthopyroxenes in

clinopyroxenes are likely related to a decrease in temperature following crystallization, suggesting chemical and mineralogical re-equilibration at different P-T conditions (Ariegite facies). As in the FMC, these petrographic characteristics indicate that the mantle cumulates record the transition from a garnet-free to a garnet-bearing facies, likely with decreasing T (France et al., 2015).

The above petrographic features and corresponding thermobarometric estimates highlight that the FMC and AVP pyroxenites record the protracted evolution of the lithospheric mantle domains, with re-equilibrations at various P-T conditions (France et al., 2015). Thus, these cumulates are now metacumulates whose mineral compositions have been modified by metamorphism and no longer represent the initial magmatic composition.

3.2. Pyroxenite trace element compositions

The chondrite-normalized REE patterns of the three FMC pyroxenites from the Devès massif are enriched in HREEs and LREEs, but depleted in middle REEs (MREEs) (see Fig. 6a, b in France et al., 2015). Thus, the chondrite-normalised REE shaped pattern decreases from the HREE to the MREE and increases from the MREE to the LREE (spoon-shaped REE pattern). The Le Pouget sample displays similar M-HREE contents, but is strongly depleted in LREEs (by up to a factor of 100 relative to M-HREEs). These enrichments in HREEs compared to MREEs attest to the initial presence of magmatic garnet. Additionally, the Devès samples are enriched in U and Th and depleted in Nb, Zr, and Hf, which, along with LREE enrichment, have been attributed to metasomatism in peridotite xenoliths of the FMC (Lenoir et al., 2000; Féménias et al., 2003; Dautria et al., 2010). Thus, the presence of these anomalies in the studied pyroxenites attest to a similar metasomatic stage in which a LREE-depleted protolith was enriched by a LREE-rich percolating agent. Moreover, sample LN78 contains amphibole-rich and amphibole-poor areas, indicating the

localized percolation of the metasomatic agent through the sample. Furthermore, clinopyroxene grains near amphiboles have REE patterns similar to those of amphiboles, i.e., highly enriched in LREEs and less depleted in HREEs than other clinopyroxenes, suggesting equilibration between the two species. Thus, FMC pyroxenites were metasomatized; amphiboles are not primary and LREE compositions do not reflect the initial magmatic composition.

The chondrite-normalized REE patterns of AVP pyroxenites display flat M-HREE patterns indicating a lack of magmatic garnet during their initial crystallization. These samples (especially YK13 and YK16) are enriched in LREEs relative to MREEs and enriched in Ba, Sr, U, and Th, and depleted in Zr and Hf relative to other trace elements with similar incompatibilities during mantle melting (see Fig. 6c, d in France et al., 2015). Similar signatures in spinel lherzolites from this region (e.g., Temdjim et al., 2004) have been attributed to metasomatic interactions, and we accordingly interpret these geochemical signatures as evidence of metasomatism (France et al., 2015).

4. Fourier-transform infrared spectroscopy

We determined the water contents of NAMs by Fourier-transform infrared spectroscopy (FTIR), a non-destructive method with a low detection limit (<1 ppm H_2O). Measurements were performed on doubly polished sections 150–300 µm thick that were cut at the Laboratoire Magmas et Volcans (Clermont-Ferrand, France) and the Université Jean Monnet (Saint Etienne, France); residue of glue used during section preparation was carefully removed in successive acetone and alcohol baths. Unpolarized and polarized spectra were acquired at the Laboratoire de Spectroscopy pour les Interactions, la Réactivité et l'Environnement (Université de Lille, France) using a Bruker Vertex 70 infrared spectrometer coupled to a HYPERION 3000 microscope and a Cassegrain 15× lens. Absorption spectra

were collected over 256 scans at 4 cm^{-1} spectral resolution between 600 and 4000 cm^{-1} in transmission mode with aperture sizes ranging between 40 × 40 μm and 100 × 100 μm depending on the size and quality (e.g., inclusions, alteration, etc.) of each mineral. The majority of analyses were performed using unpolarized infrared light, which are as reliable as polarized analyses if at least ten different grains with distinct random orientations are measured and the maximum linear unpolarized absorbance is <0.15 (Kovacs et al., 2008). To maximize the reliability of our analyses, between 16–34 grains of both clinopyroxene and orthopyroxene were analyzed in every sample (Table 3). As garnet is isotropic and anhydrous (there were no discernal absorption peaks to analyze, see section 5.3; Figs. 4, 5), only 5 analyses were performed per sample.

Because sample YK01 comprises large, cm-sized clinopyroxenes, it was not possible to analyze >10 grains; therefore, we conducted polarized analyses. Two perpendicular sections of each clinopyroxene grain were cut and several polarized analyses were performed at complementary orientations (e.g., 90°/180°, 105°/195°). Because the summed absorbances of the two sections of each grain were constant regardless of the complementary orientations used, we report results using the 90°/180° for each grain to quantify the water contents of YK01 clinopyroxenes.

All spectra were normalized to section thickness, and mean clinopyroxene and orthopyroxene spectra for each sample were calculated from the respective individual spectra. Baseline corrections for the mean spectra was performed following the procedure of Hao et al. (2014). To subtract the baseline, several methods are possible. The one used here is manual. For each considered spectrum three baselines, one optimum and two extremes are generated in order to define the uncertainty values. At least three anchor points are defined on either side of the spectrum peaks (Supplementary Fig. S2). These points are connected by a polynomial function. This method is user-dependent; however, it ensures the reliability of the choice of

the best baseline. Thus, the measurement uncertainty is defined according to the maximum and minimum areas defined under the spectra. Then, the errors due to the Bell et al. (1995) and Libowitzky and Rossman (1997) absorption coefficients are propagated until the final uncertainty obtention. The area under the OH^- peak was integrated between 3000 and 3800 cm^{-1} for clinopyroxenes and orthopyroxenes. Water concentrations were calculated from the thickness-normalized absorbances using a modified Beer-Lambert law and two calibrations: the mineral-dependent calibration of Bell et al. (1995; using integral specific absorption coefficients $I'_{Cpx} = 7.09 \pm 0.32$ and $I'_{Opx} = 14.84 \pm 0.59$ for clinopyroxene and orthopyroxene, respectively) and the wavenumber-dependent calibration of Libowitzky and Rossman (1997; using mean wavenumbers $\nu_{Cpx} = 3550$ cm^{-1} and $\nu_{Opx} = 3520$ cm^{-1}). For diopside, the wavenumber-dependent calibration is considered to be more reliable than the mineral-dependent calibration (Weis et al., 2018). However, the mineral-dependent calibration was developed using natural minerals similar to those analyzed herein and is thus particularly suitable for our purposes. Furthermore, the mineral-dependent calibration has been more widely used than the wavenumber-dependent calibration, better allowing for comparisons with literature data. Thus, although we used both calibrations, we use only the water concentrations calculated using the Bell et al. (1995) calibration for comparison with previous data. The total 2σ uncertainties on water concentrations in clinopyroxenes and orthopyroxenes are between 15 and 25% (Table 2, Supplementary Fig. S2, Fig. S4).

5. Results

Clinopyroxene and orthopyroxene water contents are presented in Table 3, and related spectra are displayed in Figs. 4 and 5. We measured core-rim profiles to demonstrate the homogeneity of water contents in clinopyroxene and orthopyroxene grains from all the studied pyroxenites (Fig. 6).

5.1. Clinopyroxene water contents

All clinopyroxenes from the AVP and Le Pouget (FMC) show similar mean spectra with absorption bands centered around ~3630 cm^{-1}, ~3530 cm^{-1}, and ~3470 cm^{-1} (Fig. 4). These bands are common in the literature (e.g., Bell et al., 1995; Bizimis and Peslier, 2015; Patkó et al., 2019), and the largest peak occurs at the highest wavenumber (~3630 cm^{-1}). Here, we refer to such spectra as 'Type 1'. In contrast, the other FMC samples (LN78, LP27, and SD53) show uncommon spectra with bands centered around ~3610 cm^{-1}, ~3518 cm^{-1}, and ~3445 cm^{-1} (Fig. 4), and the largest peak occurring at a lower wavenumber (~3518 cm^{-1}) compared to Type-1 spectra. Furthermore, the contribution of the first band, with the largest peak occurring at ~3610 cm^{-1}, to the spectra increases progressively from LN78 to Le Pouget clinopyroxenes (Fig. 4). These spectra are hereafter referred to as 'Type 2'.

Water concentrations in AVP clinopyroxenes vary between xenoliths from 386^{+78}_{-85} to 685^{+92}_{-154} ppm H_2O using the Bell et al. (1995) absorption coefficient (Fig. 7a); from 296^{+28}_{-44} to 525^{+16}_{-81} ppm H_2O using the Libowitzky and Rossman (1997) (Supplementary Fig. S3) absorption coefficient. Clinopyroxene water concentrations in samples YK01, YK03, YK05, YK12, and YK13 are homogeneous, with average values of 455 ± 24 (1σ) ppm H_2O using the Bell et al. (1995) absorption coefficient and (349 ± 19 (1σ) ppm H_2O using the Libowitzky and Rossman (1997) absorption coefficient. Only clinopyroxenes in YK16 have higher water contents of 685^{+92}_{-154} ppm H_2O using Bell et al. (1995) absorption coefficient and 525^{+16}_{-81} ppm H_2O using the Libowitzky and Rossman (1997) absorption coefficient. Unlike the AVP clinopyroxenes, water concentrations in FMC clinopyroxenes differ more markedly between xenoliths, varying from 112^{+25}_{-15} ppm H_2O in LN78 to 465^{+185}_{-100} ppm H_2O in the Le Pouget sample using Bell et al. (1995) absorption coefficient (Fig. 7a); from 85^{+9}_{-5} ppm H_2O in LN78

to 357^{+96}_{-52} ppm H_2O in the Le Pouget sample using the Libowitzky and Rossman (1997) (Supplementary Fig. S3) absorption coefficient.

5.2. Orthopyroxene water contents

Orthopyroxenes from the AVP and Le Pouget (FMC) show similar mean spectra with bands centered around ~3590 cm^{-1}, ~3518 cm^{-1}, and 3417 cm^{-1} (Fig. 4). These spectra are referred to hereafter as 'Type 1', and are the most common in the literature. Orthopyroxenes from the other FMC samples (LN78 and LP27) have spectra with only two bands centered around ~3570 cm^{-1} and ~3517 cm^{-1} (Fig. 4), which we refer to as 'Type 2' hereafter. In all orthopyroxenes, the largest peak, with the highest linear absorption, corresponds to the highest wavenumber (3590 cm^{-1} and 3570 cm^{-1} for Type-1 and Type-2 spectra, respectively).

Water concentrations in AVP orthopyroxenes (YK03, YK05, YK12, and YK13) vary between xenoliths from 124^{+15}_{-15} to 153^{+35}_{-33} ppm H_2O using Bell et al. (1995) absorption coefficient (Fig. 7b); from 160^{+6}_{-8} to 201^{+26}_{-30} ppm H_2O using the Libowitzky and Rossman (1997) (Supplementary Fig. S3) absorption coefficient, but are homogeneous with an average value of 143 ± 13 (1σ) ppm H_2O using Bell et al. (1995) absorption coefficient and 184 ± 17 (1σ) ppm H_2O using the Libowitzky and Rossman (1997) absorption coefficient. Water concentrations in FMC orthopyroxenes (LN78, LP27, and Le Pouget) vary from 61^{+22}_{-13} ppm H_2O in LN78 to 104^{+14}_{-18} ppm H_2O in Le Pouget using Bell et al. (1995) absorption coefficient (Fig. 7b); from 78^{+19}_{-12} ppm H_2O in LN78 to 135^{+6}_{-14} ppm H_2O in Le Pouget using the Libowitzky and Rossman (1997) (Supplementary Fig. S3) absorption coefficient. Although SD53 (FMC) contains orthopyroxenes, they were not analyzed because they show secondary fluid inclusions and some alteration features.

5.3. Garnet water contents

None of the garnet spectra show OH bands between 3000 and 3800 cm^{-1} (Fig. 4). Water concentrations in these garnets are therefore below the FTIR detection limit for garnet and this range of sample thickness (<0.5 ppm H_2O; Bizimis and Peslier, 2015). Therefore, we hereafter consider the studied garnets to be anhydrous. In the Le Pouget sample, rare areas near the edges of some garnets or in fracture zones present a small peak between 3000 and 3800 cm^{-1} that may result from a late episode of fluid diffusion through fractures (Suzuki and Nakashima, 2004). Despite this event, the cores of those grains remain anhydrous.

6. Discussion

To better understand the distribution of water in the lithospheric mantle and its implications, we divide the discussion of our results into in three parts. We first discuss whether the quantified water contents represent lithospheric mantle signatures or were modified during xenolith transport to the surface (section 6.1). We then explore the potential influence of metasomatism on the lithospheric water contents (section 6.2), and finally discuss the use of H_2O/Ce to track the influence of pyroxenite during magma genesis (section 6.3).

6.1. Water contents: Mantle signature preservation and whole-rock water concentrations

A key concern when studying water systematics in NAMs is whether the xenoliths retained their primary water contents; here, that is whether the pyroxenites reliably preserve mantle water from before their ascent to the surface in the host magma, or if the mantle water was modified during ascent. Indeed, the solubility of water varies with pressure and temperature, and its diffusivity in the melt and minerals may enable quick re-equilibration

with the host magma at magmatic temperatures, even at the timescale of an individual eruption (e.g., Zhao et al., 2004; Ingrin and Blanchard, 2006; Demouchy and Bolfan-Casanova, 2016). Moreover, degassing can potentially disturb xenolith water contents. Hence, mineral water contents, especially olivine, could be disturbed during xenolith ascent and emplacement (e.g., Demouchy et al., 2006, 2015; Peslier and Bizimis, 2015; Hao et al., 2016a). Here, we consider three criteria to determine if the pyroxenite water contents effectively document water contents in the lithospheric mantle.

First, our profile analyses highlight the homogeneity of clinopyroxene, orthopyroxene, and garnet grains in all studied pyroxenites (Fig. 6). Indeed, the water contents of pyroxene cores and rims are identical within uncertainties, whereas the diffusion of H into or out of pyroxene would result in increased or decreased rim water contents, respectively. Consequently, there is no evidence that hydrogen diffused into or out of the FMC and AVP pyroxenes at the timescale of magma ascent and emplacement.

Second, in the FMC pyroxenites, orthopyroxene and clinopyroxene water contents correlate with their major element concentrations, such as Mg# (R^2 = 0.91) and Ca (R^2 = 0.99) in clinopyroxene (Fig. 8a, b) and Mg# (R^2 = 0.99) in orthopyroxene (Fig. 8c). The diffusivities of these major elements preclude their re-equilibration at the grain scale over periods characteristic of mantle xenolith ascent times (a few hours to days; e.g., Demouchy et al., 2006). Therefore, the water and major element concentrations in FMC pyroxenites are interdependent and consistent with water contents at equilibrium conditions prior sampling by the magma. In contrast, there are no such correlations in AVP pyroxenites (Fig. 8), indicating that their water was likely not acquired during the stage of major element equilibration or at least much less sensitive to these changes.

Lastly, clinopyroxenes in FMC and AVP pyroxenites contain 1.5–3.5 times more water than orthopyroxenes from the same sample (Fig. 9), consistent with the range of water

partition coefficients between clinopyroxene and orthopyroxene ($D_{H_2O}^{Cpx-Opx}$) determined in natural samples: 1.5–3.5 (Warren and Hauri, 2014; Bizimis and Peslier, 2015; Demouchy and Bolfan-Casanova, 2016; Demouchy et al., 2017; Peslier et al., 2017; Xia et al., 2017; Hao et al., 2018; Li et al., 2018). Hence, clinopyroxene and orthopyroxene water contents are considered to be in equilibrium for all samples studied herein.

Based on these three arguments, the FMC and AVP pyroxenites likely preserved their lithospheric water contents during xenolith ascent. Based on this assumption, bulk-rock water concentrations can be estimated by considering the modal percentages and water contents of each mineral. This calculation shows that bulk-rock AVP pyroxenite water concentrations are homogeneous with an average value of 309 ± 95 (1σ) ppm H_2O (ranging from 231^{+47}_{-51} to 480^{+64}_{-108} ppm H_2O using the Bell et al. (1995) absorption coefficient. Bulk-rock water concentrations of FMC pyroxenites vary from 58^{+15}_{-9} ppm H_2O for LN78 to 287^{+113}_{-61} ppm H_2O for the Le Pouget sample (Table 3, Fig. 7c).

6.2. Influence of metasomatism on water contents: unaffected AVP pyroxenites vs dehydrated FMC pyroxenites

Because hydrogen is both volatile and incompatible, both modal and cryptic metasomatism likely can affect the water contents of upper mantle minerals. Nevertheless, Denis et al. (2015) showed that neither modal (e.g., presence of hydrated minerals such as amphibole) nor cryptic (e.g., LREE and MREE enrichments) metasomatic interactions have had a clear effect on the water contents of FMC peridotite xenoliths. They suggested that only high-melt/rock-ratio interactions have the potential to dehydrate xenoliths (Denis et al., 2018). In contrast, other studies have attributed high water concentrations in pyroxenites and peridotites to metasomatic agents (e.g., Peslier and Bizimis, 2015; Li et al., 2018; Patkó et al.,

2019). In this perspective, we explore the influence of metasomatism on AVP and FMC pyroxenite water contents to determine if they represent those acquired during metasomatism or rather document the subsequent equilibration conditions of the mantle metacumulates. Several lines of evidence indicate that some degree of metasomatism occurred after igneous crystallization, such as bulk-rock and mineral LREE enrichments associated with specific elemental enrichments or depletions (e.g., U enrichments and depleted high field strength element concentrations in the FMC; U and Th enrichments in the AVP); these features are similar to geochemical signatures of the host peridotitic lithospheric domains that have been attributed to metasomatism (e.g., Lenoir et al., 2000; Féménias et al., 2003; Temdjim et al., 2004; Dautria et al., 2010).

Geochemical tracers can be used to identify and characterize metasomatic agents. The Cameroon lithospheric mantle, especially beneath the AVP, experienced metasomatism during the early break-up of Pangea around 200 Ma, which accounts for the incompatible element enrichments in related peridotites (Lee et al., 1996; Temdjim et al., 2004; Njombie et al., 2018). The studied AVP pyroxenites are similarly enriched in LREEs, U, and Th relative to MREEs and other incompatible trace elements, and therefore also experienced metasomatism (France et al., 2015). Two types of mantle-melt interactions are recorded in lherzolites from the AVP: (i) cryptic metasomatism and trace element enrichments are attributed to a regional mantle plume and the percolation of hydrous silicate melts, whereas (ii) enrichments in CaO relative to Al_2O_3 during refertilization are attributed to the percolation of carbonatite or carbonated silicate melts (Njombie et al., 2018).

The La_N/Sm_N ratio (the subscript 'N' denotes chondrite-normalized values; Anders and Grevesse, 1989) is widely used to identify mantle metasomatism, whereas the Ti/Eu ratio is a good proxy for carbonatitic metasomatism (Ashley et al., 2020), which is characterized by Ti, Zr, and Hf depletions relative to REEs. Indeed, as Ti, Zr and Hf are less incompatible than

REEs in a carbonatic melt, the mineral, which interacts with this carbonatitic melt would record its signature (Ashley et al., 2020). This correlation relies on the corresponding partition coefficients that imply that REE are strongly enriched in carbonatite melts when HFSE (Ti, Nb-Ta, Zr-Hf) are strongly depleted (e.g., Coltorti et al., 1999; Martin et al., 2013). The studied AVP pyroxenites likely record a metasomatic stage related to hydrous silicate melts because Ti/Eu and La_N/Sm_N are not correlated (Fig. 10). Thus, to track the metasomatic influence on the pyroxenite water contents, we plotted clinopyroxene and whole-rock water concentrations against La_N/Sm_N (Fig. 11a, b). Clinopyroxene water contents are not correlated with La_N/Sm_N whereas whole-rock contents show a rough positive correlation ($R^2 = 0.57$, Fig. 11b). The whole-rock enrichments in LREEs relative to MREEs in these samples might be related to the widespread metasomatic stage that affected the Cameroon lithospheric domain (Lee et al., 1996; Temdjim et al., 2004; France et al., 2015; Njombie et al., 2018). Nevertheless, because clinopyroxene water concentrations do not correlate with tracers of metasomatism, we propose that the rough whole-rock correlation reflects the modal composition of the pyroxenites and not a metasomatic event. Indeed, the most water-rich AVP pyroxenite YK16 contains the most clinopyroxene (the most hydrous mineral phase present). Furthermore, samples YK01, YK05, and YK16 contain megacrysts, decreasing the reliability of the results. Therefore, we consider that all AVP pyroxenites have roughly similar water contents that were not affected by metasomatism by the hydrous silicate melts, a result similar to what Denis et al. (2018) observed in the FMC. The relative homogeneity of water contents of AVP pyroxenites likely documents a previous equilibration stage in the lithosphere during their PT evolution that is not directly related to metasomatism.

The lithospheric mantle beneath the FMC also experienced metasomatic interactions: the northern domain was metasomatized by carbonatitic melts (Lenoir et al., 2000; Wittig et al., 2007), whereas the southern domain was metasomatized by both hydrous silicate melts

and carbonatitic melts (Wittig et al., 2007; Gu et al., 2018). The FMC samples studied herein show a robust correlation between La_N/Sm_N and Ti/Eu (R^2 = 0.88, Fig. 10), consistent with recent evidence of carbonatitic metasomatism in the FMC (e.g. Gu et al., 2018). The negative correlations between clinopyroxene and whole-rock La_N/Sm_N ratios and water concentrations (Fig. 11a, b) can be interpreted as indicative of a common process for LREE enrichment and water depletion. Indeed, according to Keppler (2003) and Sokol et al. (2013), carbonatitic melts can be considered as "dry" metasomatic agents with low water activity in the melt, and have the potential to extract water from even water-poor rocks such as peridotite or pyroxenite.

The presence of amphiboles could also explain the dehydration of FMC pyroxenes. Indeed, the metasomatism would have stabilized amphibole, which by being OH-rich, resulted in dehydration of these pyroxenes. However, Denis et al (2015) showed that the presence of amphibole does not affect the water content of NAMs. There is also a continuous variation in water content between the four samples, from the OH-rich sample (Le Pouget) to the OH-poor sample (LN78). Moreover, LP27 also contains little water while no amphibole is present. Finally, all samples from Cameroon (but YK01) contain small amounts of amphibole, and all of them are OH-rich. Thus, the dehydration of FMC pyroxenites is preferentially due to the carbonatitic metasomatism.

Furthermore, the strength of the metasomatic imprint (i.e., the degrees of LREE enrichment and Ti/Eu depletion) correlates with the type of FTIR spectra observed (type 1 vs. type 2): the more pronounced the carbonatitic metasomatic imprint, the weaker the high-wavenumber water band (type 2, see the most metasomatized sample LN78 in Fig. 4). The spectral signature of water in minerals is characterized by various bands, each representing precise vibrational interactions, and the several hydrogen storage defects present in the pyroxene lattice account for the various bands observed between 3000 and 4000 cm^{-1} (Ingrin

and Skogby, 2000). Several processes can explain the incorporation of water in NAM structures, including cation vacancies (e.g., $2H^+$ vs. Mg^{2+} or $4H^+$ vs. Si^{4+}), charge balance (e.g., $Al^{3+} + H^+$ vs. Si^{4+}), and redox reactions ($Fe^{3+} - O^{2+} + 1/2H_2 = Fe^{2+} + OH^-$). However, according to several authors (e.g., Skogby, 1994; Yang et al., 2019) there is no clear correlation between band positions and clinopyroxene chemical composition. It is therefore difficult to attribute specific band (between 3000 and 4000 cm^{-1}) to specific OH locations in the crystalline structure. We suggest here that the carbonatitic metasomatism of the FMC pyroxenites preferentially dehydrated a specific OH site in the pyroxene structure, resulting in the uncommon type-2 spectra observed herein (Ingrin et al., 2019).

Type-2 spectra have also been reported scarcely in the literature and were associated with low structural hydroxyl contents (<360 ppm: Patkó et al., 2019), in agreement with our findings (Denis et al., 2018; Gu et al., 2018; Patko et al., 2019). However, contrary to the observations of Patkó et al. (2019), there is no correlation of type-2 spectra (and related low water content) with anomalously high hydroxyl partition coefficients between clinopyroxene and orthopyroxene: the ratio of clinopyroxene to orthopyroxene water contents in LN78 and LP27 are within 1.5–3.5, matching literature data (Fig. 9; Peslier et al., 2002, 2012; Peslier, 2010; Xia et al., 2010, 2013; Yu et al., 2011; Hao et al., 2012, 2014, 2016a, 2016b; Doucet et al., 2014; Warren and Hauri, 2014; Bizimis and Peslier, 2015; Demouchy et al., 2015; Hui et al., 2015; Li et al., 2015; Peslier and Bizimis, 2015; Denis et al., 2018; Hao et al., 2018). However, because Patkó et al. (2019) focused on peridotites whereas we focus on pyroxenites, differences in mineral partitioning or exchanges may explain the different observed partition coefficients. Several other parameters could also influence structural hydroxyl contents, and thus the observed spectra, such as oxidation caused by infiltration of the host magma (which in some cases, lowers the solubility of water in minerals, resulting in dehydration during peridotite partial melting; Peslier et al., 2002; Tollan and Hermann, 2019) or decreased water

activity due to the infiltration of a "dry" agent (Patkó et al., 2019). Because the whole-rock water contents of FMC and AVP pyroxenites are not correlated with redox state (France et al., 2015; Supplementary Fig. S1; $R^2 = 0.01$ and $R^2 = 0.13$ respectively), the infiltration of an oxidized melt seems unlikely in the case of the FMC pyroxenites. Finally, because the water contents and major element concentrations (e.g., Al or Mg#) of FMC pyroxenites are correlated (see section 5.1), the water contents are negatively correlated with the major element equilibration temperatures determined by France et al. (2015): the least hydrous and most metasomatized samples have the highest equilibrium temperatures (Table 2, Fig. 12), consistent with their partial dehydration during the metasomatism of the FMC lithospheric mantle by a hot carbonatitic melt or fluid.

In conclusion, FMC pyroxenites were metasomatized by a carbonatitic agent (Wittig et al., 2007; Gu et al., 2018) and AVP pyroxenites by a hydrous silicate one (Njombie et al., 2018). These interactions modified their major and trace element compositions and the carbonatitic melt likely dehydrated the FMC pyroxenites, seemingly from a specific structural site, resulting in their unusual spectral signatures.

6.3. Pyroxenites, metasomatism, H_2O/Ce, and basalt sources

Pyroxenites are generally more water-rich than peridotites (Fig. 1) and are a key lithology for quantifying the water distribution in the upper mantle. Despite their relatively low abundance in mantle domains, their lower solidus temperatures relative to peridotites result in their disproportionate implication in magma genesis (e.g., Hirschmann and Stolper, 1996; Bizimis and Peslier, 2015). Nonetheless, quantifying their importance in magma genesis relative to peridotites has remained elusive because the major element compositions of the melts produced by melting each lithology are relatively similar (e.g., Le Roux et al., 2010; Lambart et al., 2013). Although radiogenic isotopes (e.g., Sr-Nd-Pb) are powerful

tracers of the involvement of mantle reservoirs evolving separately over billions of years (e.g., the DMM, HIMU, or EM reservoirs), only a few minor elements have proven reliable for tracking mantle compositional heterogeneities such as the presence of pyroxenites in basalt mantle sources. For example, the implication of pyroxenites in mantle melting is reflected by higher Ni/Mg and lower Mn/Fe or Ca/Fe ratios in olivine phenocrysts or by higher Zn/Fe and Ge/Si ratios in the formed basalts (Sobolev et al., 2007; Le Roux et al., 2010; Yang et al., 2020).

Alternatively, H_2O/Ce ratios may document the chemical composition of basalt mantle sources (Michael, 1995). Indeed, because H_2O and Ce have similar partition coefficients during peridotite mantle melting, the H_2O/Ce ratio is expected to remain unchanged during this process, allowing mantle water contents to be estimated from basalts (Dixon et al., 1988; Michael, 1988, 1995). This was confirmed by Hauri et al. (2006) who showed that, despite the different H_2O and Ce partition coefficients for olivine, clinopyroxene, orthopyroxene, and garnet, the overall melting process buffers the H_2O/Ce ratio, which remains almost constant during melting. Bizimis and Peslier (2015) also suggested that the implication of low H_2O/Ce ratio garnet pyroxenites (H_2O/Ce < 200; [H_2O] > 350 ppm) in mantle melting could account for the low H_2O/Ce ratios of some fertile magmas (Hawaii, Samoa, Society). Relying on those important results and based on the observation that pyroxenites from other settings are also characterized by low H_2O/Ce ratios (e.g., Hao et al., 2018; Li et al., 2018; Fig. 13), it seems plausible that the H_2O/Ce ratio of basalts might track the involvement of pyroxenite in their genesis. We here explore this possibility in light of our new results.

Because the partition coefficients of H_2O and Ce vary among minerals, the evolution of the H_2O/Ce ratio during the melting of peridotite or pyroxenite also depends on mineralogical and modal compositions. Indeed, although Hauri et al. (2006) showed that the

H_2O/Ce ratio is buffered and remains almost constant during peridotite melting, this may not be the case for pyroxenite. The use of basalt H_2O/Ce ratios to quantify the water content of the mantle source may thus be inappropriate when pyroxenitic lithologies are involved. To test this, we calculated the H_2O and Ce partition coefficients for bulk-rock pyroxenites based on literature constraints and mineral partition coefficients. $D_{H_2O}^{Cpx-melt}$ varies between 0.015 and 0.019 among different samples and $D_{H_2O}^{Opx-melt}$ between 0.009 and 0.015 (compositionally dependent values from O'Leary et al., 2010; Table 3). $D_{H_2O}^{Garnet-melt}$ = 0.0032 and does not vary with pressure (Novella et al., 2014), representing the value at upper mantle depths. The partition coefficients of Ce between the liquid and constituent minerals are $D_{Ce}^{Cpx-melt}$ = 0.0858 (Hart and Dunn, 1993), $D_{Ce}^{Opx-melt}$ = 0.0017 (Adam and Green, 2006), and $D_{Ce}^{Garnet-melt}$ = 0.0034 (Klemme et al., 2002). Hence, $D_{H_2O}^{Pyroxenite-melt}$ varies between 0.011 and 0.014 and $D_{Ce}^{Pyroxenite-melt}$ between 0.038 and 0.068 depending on modal composition. Therefore, we reach the same conclusions as Bizimis and Peslier (2015): Ce is 4–5 times more compatible than H_2O in pyroxenites, and the H_2O/Ce ratio is likely modified during the melting process (e.g., increasing during partial melting).

To verify the efficiency of this tool as a source tracer, we ran a non-modal, incremental batch-melting model using modal mineralogies representative of our samples and assuming similar melting proportions of the main phases (1/3 clinopyroxene, 1/3 orthopyroxene, and 1/3 garnet; Fig. 14). At low degrees of melting, H_2O/Ce can be up to three times the starting values of the studied pyroxenites, especially for the Le Pouget sample. With increasing degrees of partial melting, the ratios reach values similar to those of the melting pyroxenite at ~10% melting (Fig. 14). Thus, at least 10% partial melting of the pyroxenite assemblage is required to obtain a H_2O/Ce similar to that of the magma sources. In the case of peridotites, such differences between the H_2O and Ce partition coefficients, and thus between

the H_2O/Ce ratios of the partial melting products and the source, are only apparent at <3% partial melting (Hauri et al., 2006), and the H_2O/Ce ratios of basalts can thus be used to estimate the water content of the mantle source at higher degrees of melting. Because pyroxenites are fertile lithologies, e.g., up to 20% pyroxenite partial melting can be attained before the onset of lherzolite melting (Hirschmann and Stolper, 1996), it is likely that pyroxenite signatures can be detected in basalts. It follows that, if pyroxenites display different H_2O/Ce ratios than peridotites, the H_2O/Ce ratio can be used as a tracer of pyroxenites in the mantle source, and thus to attempt to quantify the involvement of pyroxenites during magmas genesis. However, both the AVP and FMC pyroxenites have H_2O/Ce ratios spanning a wider range of values (from 30^{+8}_{-5} to $2{,}388^{+945}_{-512}$) than in previous studies (Bizimis and Peslier, 2015; Hao et al., 2018; Li et al., 2018), and H_2O contents varying from 58^{+15}_{-9} to 480^{+64}_{-108} ppm (Fig. 13). Thus, most of the variability of H_2O/Ce ratios herein is governed by variations in Ce content (and thus by metasomatism), and the highest H_2O/Ce ratio is observed for the Ce-poor Le Pouget sample, the least metasomatized pyroxenite from the FMC. The range of H_2O/Ce ratios in the studied pyroxenites is larger than that reported for the peridotitic mantle, reducing the utility of H_2O/Ce for tracking pyroxenites in the magma source.

The question that remains is: why are such extreme H_2O/Ce ratios (e.g., $2{,}388^{+945}_{-512}$) not observed in lavas at the surface when pyroxenites are generally more involved than peridotites in magma genesis. Although H_2O/Ce systematics have not been studied in the FMC, magmas erupted at the surface likely result from the aggregation of heterogeneous magma batches formed by the partial melting of different mantle domains (e.g., Grove et al., 1992; Morgan et al., 1992; Saal et al., 1998; Koornneef et al., 2019). Lava compositions therefore likely represent the product of magma mixing, with little chance of preserving extreme values, especially in the case of incompatible elements such as Ce (e.g., Stracke et

al., 2019). For example, Stracke et al. (2019) identified depleted magmatic melt inclusions in basaltic lavas from the Azores, although this heterogeneity was not detected in bulk analyses. Under similar conditions, the melting of pyroxenites similar to the Le Pouget sample might not be detected in erupting magmas because such depleted melts do not directly rise to the surface, but rather mix with various magma batches formed by the melting of surrounding peridotites. Finally, given the H_2O/Ce variations recorded in the studied pyroxenite samples (from 30^{+8}_{-5} to $2{,}388^{+945}_{-512}$) and the striking effect of metasomatism on their signature, the reliability of the H_2O/Ce systematic to track the presence of pyroxenites in magma sources worldwide is limited; it is most applicable in areas where the H_2O/Ce ratios of pyroxenites differ markedly from those of peridotites (e.g., Bizimis and Peslier, 2015).

7. Conclusions

This study reports new FTIR data characterizing water contents in the continental lithospheric mantle beneath the FMC (France) and AVP (Cameroon). We quantified bulk-rock and NAM water contents in pyroxenites that represent mantle heterogeneities in the lithospheric domains of each region. NAMS are homogeneous at the grain and sample scales (no evidence of diffusion) and in equilibrium according to available partitioning coefficients, and water contents correlate with major element concentrations or equilibrium temperature for FMC pyroxenites. Therefore, we interpret that the water contents of FMC and AVP pyroxenites were not noticeably modified during xenolith ascent and emplacement and are thus representative of lithospheric conditions.

Correlations between water concentration and proxies of metasomatism suggest that the FMC pyroxenite water contents were modified by metasomatic agents in the lithospheric mantle. Based on previous geochemical constraints on the metasomatic agents affecting FMC pyroxenites, we conclude that a carbonatitic metasomatic agent caused the dehydration of the

pyroxenite minerals. Based on their peculiar FTIR absorption spectra, we suggest that this dehydration preferentially affected specific OH storage sites in pyroxenes. The water contents of AVP pyroxenites have not been noticeably affected by metasomatism.

Finally, we investigated the validity of the H_2O/Ce systematic in our samples, which has been proposed as a tool for tracking the involvement of pyroxenite during magma genesis. Based on our new analyses we conclude that the increased range of H_2O/Ce ratios for bulk-rock pyroxenites limits the utility of this parameter as a magma source tracer.

Acknowledgments:

We express our warm thanks to Colette Guillaud for the quality of her double polished thin sections. We thank Isabelle De Waele for her help with FTIR measurements at Université de Lille. We also thank J.C. Vilmhot and D. Velde, who provided garnet pyroxenite samples from the Devès Massif and valuable geochemical data, J.P. Lorand for providing the Le Pouget sample from the MNHN-Paris collection, and R. Temdjim & P. Boivin for sharing the Cameroon samples with us. Etienne Deloule is thanked for fruitful discussions. Istvan Kovacs, Michael Bizimis, Debajyoti Paul, Anne Peslier, Dhilip Kumar, Karen H. Johannesson and an anonym reviewer are thanked for their constructive comments. This work was supported by the TelluS Program of CNRS-INSU through grant provided to J. Ingrin. This is CRPG contribution n°xxxx.

Research Data

Research Data associated with this article can be accessed at doi:10.17632/jc46vyk76v.1 on Mendeley Data.

Supplementary data

Supplementary Figure S1

Supplementary Figure S2

Supplementary Figure S3

Supplementary Figure S4

References

Adam, J., Green, T., 2006. Trace element partitioning between mica- and amphibole-bearing garnet lherzolite and hydrous basanitic melt: 1. Experimental results and the investigation of controls on partitioning behaviour. Contributions to Mineralogy and Petrology 152, 1–17. doi:10.1007/s00410-006-0085-4

Allègre, C.J., Turcotte, D.L., 1986. Implications of a two-component marble-cake mantle. Nature 323, 123-127. doi:10.1038/323123a0

Anders, E., Grevesse, N., 1989. Abundances of the elements: Meteoritic and solar. Geochimica et Cosmochimica Acta 53, 197–214. doi:10.1016/0016-7037(89)90286-X

Ashley, A.W., Bizimis, M., Peslier, A.H., Jackson, M., Konter, J., 2020. Metasomatism and Hydration of the Oceanic Lithosphere: a Case Study of Peridotite Xenoliths from Samoa. J. Petrol. 61, egaa028

Asimow, P.D., Dixon, J.E., Langmuir, C.H., 2004. A hydrous melting and fractionation model for mid-ocean ridge basalts: Application to the Mid-Atlantic Ridge near the Azores: Hydrous Melting and Fractionation. Geochemistry, Geophysics, Geosystems 5, Q01E16. doi:10.1029/2003GC000568

Bell, D.R., Rossman, G.R., 1992. Water in Earth's Mantle: The Role of Nominally Anhydrous Minerals. Science 255, 1391–1397. doi:10.1126/science.255.5050.1391

Bell, D.R., Ihinger, P.D., Rossman, G.R., 1995. Quantitative analysis of trace OH in garnet

and pyroxenes. American Mineralogist 80, 465–474. doi:10.2138/am-1995-5-607

Beran, A., Libowitzky, E., 2006. Water in Natural Mantle Minerals II: Olivine, Garnet and Accessory Minerals. Reviews in Mineralogy and Geochemistry 62, 169–191. doi:10.2138/rmg.2006.62.8

Bizimis, M., Peslier, A.H., 2015. Water in Hawaiian garnet pyroxenites: Implications for water heterogeneity in the mantle. Chemical Geology 397, 61–75. doi:10.1016/j.chemgeo.2015.01.008

Bolfan-Casanova, N., Muñoz, M., McCammon, C., Deloule, E., Ferot, A., Demouchy, S., France, L., Andrault, D., Pascarelli, S., 2012. Ferric iron and water incorporation in wadsleyite under hydrous and oxidizing conditions: a XANES, Mössbauer, and SIMS study. American Mineralogist, 97: 1483-1493, doi: 10.2138/am.2012.3869

Borghini, G., Rampone , E., Zanetti, A., Class, C., Cipriani, A., Hofmann, A.W., Goldstein, S.L., 2016. Pyroxenite Layers in the Northern Apennines' Upper Mantle (Italy)—Generation by Pyroxenite Melting and Melt Infiltration. Journal of Petrology 57, 625-653. doi:10.1093/petrology/egw074

Cabral, R.A., Jackson, M.G., Koga, K.T., Rose-Koga, E.F., Hauri, E.H., Whitehouse, M.J., Price, A.A., Day, J.M.D., Shimizu, N., Kelley, K.A., 2014. Volatile cycling of H_2O, CO_2, F, and Cl in the HIMU mantle: A new window provided by melt inclusions from oceanic hot spot lavas at Mangaia, Cook Islands. Geochemistry, Geophysics, Geosystems 15, 4445–4467. doi:10.1002/2014GC005473

Castaing, C., Feybesse, J.L., Thiéblemont, D., Triboulet, C., Chèvremont, P., 1994. Palaeogeographical reconstructions of the Pan-African/Brasiliano orogen: closure of an oceanic domain or intracontinental convergence between major blocks? Precambrian Research 69, 327–344. doi:10.1016/0301-9268(94)90095-7

Coltorti, M., Bonadiman, C., Hinton, R.W., Siena, F., Upton, B.G.J., 1999. Carbonatite

Metasomatism of the Oceanic Upper Mantle: Evidence from Clinopyroxenes and Glasses in Ultramafic Xenoliths of Grande Comore, Indian Ocean. Journal of Petrology 40, 133-165. doi:10.1093/petroj/40.1.133

Dautria, J.M., Liotard, J.M., Bosch, D., Alard, O., 2010. 160 Ma of sporadic basaltic activity on the Languedoc volcanic line (Southern France): A peculiar case of lithosphere–asthenosphere interplay. Lithos 120, 202-222. doi:10.1016/j.lithos.2010.04.009

Demouchy, S., Jacobsen, S.D., Gaillard, F., Stern, C.R., 2006. Rapid magma ascent recorded by water diffusion profiles in mantle olivine. Geology 34, 429. doi:10.1130/G22386.1

Demouchy, S., Ishikawa, A., Tommasi, A., Alard, O., Keshav, S., 2015. Characterization of hydration in the mantle lithosphere: Peridotite xenoliths from the Ontong Java Plateau as an example. Lithos 212–215, 189–201. doi:10.1016/j.lithos.2014.11.005

Demouchy, S., Bolfan-Casanova, N., 2016. Distribution and transport of hydrogen in the lithospheric mantle: A review. Lithos 240–243, 402–425. doi:10.1016/j.lithos.2015.11.012

Demouchy, S., Shcheka, S., Denis, C.M.M., Thoraval, C., 2017. Subsolidus hydrogen partitioning between nominally anhydrous minerals in garnet-bearing peridotite. American Mineralogist 102, 1822–1831. doi:10.2138/am-2017-6089

Denis, C.M.M., Alard, O., Demouchy, S., 2015. Water content and hydrogen behaviour during metasomatism in the uppermost mantle beneath Ray Pic volcano (Massif Central, France). Lithos 236–237, 256–274. doi:10.1016/j.lithos.2015.08.013

Denis, C.M.M., Demouchy, S., Alard, O., 2018. Heterogeneous hydrogen distribution in orthopyroxene from veined mantle peridotite (San Carlos, Arizona): Impact of melt-rock interactions. Lithos 302–303, 298–311. doi:10.1016/j.lithos.2018.01.007

Dixon, J.E., Stolper, E., Delaney, J.R., 1988. Infrared spectroscopic measurements of CO_2 and H_2O in Juan de Fuca Ridge basaltic glasses. Earth and Planetary Science letters, 90

87-104. doi:10.1016/0012-821X(88)90114-8

Dixon, J.E., Clague, D.A., 2001. Volatiles in Basaltic Glasses from Loihi Seamount, Hawaii: Evidence for a Relatively Dry Plume Component. Journal of Petrology 42, 627–654. doi:10.1093/petrology/42.3.627

Dixon, J.E., Leist, L., Langmuir, C., Schilling, J.-G., 2002. Recycled dehydrated lithosphere observed in plume-influenced mid-ocean-ridge basalt. Nature 420, 385–389. doi:10.1038/nature01215

Doucet, L.S., Peslier, A.H., Ionov, D.A., Brandon, A.D., Golovin, A.V., Goncharov, A.G., Ashchepkov, I.V., 2014. High water contents in the Siberian cratonic mantle linked to metasomatism: An FTIR study of Udachnaya peridotite xenoliths. Geochimica et Cosmochimica Acta 137, 159–187. doi:10.1016/j.gca.2014.04.011

Downes, H., 2007. Origin and significance of spinel and garnet pyroxenites in the shallow lithospheric mantle: Ultramafic massifs in orogenic belts in Western Europe and NW Africa. Lithos 99, 1-24. doi:10.1016/j.lithos.2007.05.006

Fei, H., Wiedenbeck, M., Yamazaki, D., Katsura, T., 2013. Small effect of water on upper-mantle rheology based on silicon self-diffusion coefficients. Nature 498, 213–215. doi:10.1038/nature12193

Féménias, O., Coussaert, N., Bingen, B., Whitehouse, M., Mercier, J.C.C., Demaiffe, D., 2003. A Permian underplating event in late- to post-orogenic tectonic setting. Evidence from the mafic–ultramafic layered xenoliths from Beaunit (French Massif Central). Chemical Geology 199, 293-315. doi:10.1016/S0009-2541(03)00124-4

France, L., Chazot, G., Kornprobst, J., Dallai, L., Vannucci, R., Grégoire, M., Bertrand, H., Boivin, P., 2015. Mantle refertilization and magmatism in old orogenic regions: The role of late-orogenic pyroxenites. Lithos 232, 49–75. doi:10.1016/j.lithos.2015.05.017

Gonzaga, R.G., Lowry, D., LeRoex, A., Schulze, D., Menzies, M.A., 2010. Eclogites and

garnet pyroxenites: Similarities and differences. Journal of Volcanology and Geothermal Research 190, 235-247. doi:10.1016/j.jvolgeores.2009.08.022

Green, D.H., 2015. Experimental petrology of peridotites, including effects of water and carbon on melting in the Earth's upper mantle. Physics and Chemistry of Minerals 42, 95-122. doi:10.1007/s00269-014-0729-2

Green, D.H., Hibberson, W.O., Kovács, I., Rosenthal, A., 2010. Water and its influence on the lithosphere–asthenosphere boundary. Nature 467, 448-451. doi:10.1038/nature09369

Grove, T.L., Kinzler, R.J., Bryan, W.B., 1992. Fractionation of mid-ocean ridge basalt (MORB). Geophysical Monograph Series 71. doi:10.1029/GM071p0281

Gu, X., Deloule, E., France, L., Ingrin, J., 2016. Multi-stage metasomatism revealed by trace element and Li isotope distributions in minerals of peridotite xenoliths from Allègre volcano (French Massif Central). Lithos 264, 158–174. doi:10.1016/j.lithos.2016.07.019

Gu, X., Ingrin, J., Deloule, E., France, L., Xia, Q., 2018. Metasomatism in the sub-continental lithospheric mantle beneath the south French Massif Central: Constraints from trace elements, Li and H in peridotite minerals. Chemical Geology 478, 2–17. doi:10.1016/j.chemgeo.2017.08.006

Hao, Y., Xia, Q., Liu, S., Feng, M., Zhang, Y., 2012. Recognizing juvenile and relict lithospheric mantle beneath the North China Craton: Combined analysis of H_2O, major and trace elements and Sr–Nd isotope compositions of clinopyroxenes. Lithos 149, 136–145. doi:10.1016/j.lithos.2012.03.013

Hao, Y., Xia, Q., Li, Q., Chen, H., Feng, M., 2014. Partial melting control of water contents in the Cenozoic lithospheric mantle of the Cathaysia block of South China. Chemical Geology 380, 7–19. doi:10.1016/j.chemgeo.2014.04.017

Hao, Y.-T., Xia, Q.-K., Jia, Z.-B., Zhao, Q.-C., Li, P., Feng, M., Liu, S.-C., 2016a. Regional

heterogeneity in the water content of the Cenozoic lithospheric mantle of Eastern China: Heterogeneous Water content in Mantle. Journal of Geophysical Research: Solid Earth 121, 517–537. doi:10.1002/2015JB012105

Hao, Y.-T., Xia, Q.-K., Tian, Z.-Z., Liu, J., 2016b. Mantle metasomatism did not modify the initial H_2O content in peridotite xenoliths from the Tianchang basalts of eastern China. Lithos 260, 315–327. doi:10.1016/j.lithos.2016.06.003

Hao, Y.-T., Li, P., Coltorti, M., Xia, Q.-K., 2018. Variations in the H_2O Content and H_2O/Ce Ratio of Mantle Pyroxenites: Implications for Enriched Components in the Mantle. Journal of Geophysical Research: Solid Earth 123, 5628–5643. doi:10.1029/2018JB015854

Hart, S.R., Dunn, T., 1993. Experimental cpx/melt partitioning of 24 trace elements. Contributions to Mineralogy and Petrology 113, 1–8. doi:10.1007/BF00320827

Hauri, E., Gaetani, G., Green, T., 2006. Partitioning of water during melting of the Earth's upper mantle at H_2O-undersaturated conditions. Earth and Planetary Science Letters 248, 715–734. doi:10.1016/j.epsl.2006.06.014

Hirschmann, M.M., Stolper, E.M., 1996. A possible role for garnet pyroxenite in the origin of the "garnet signature" in MORB. Contributions to Mineralogy and Petrology 124, 185–208. doi:10.1007/s004100050184

Hirth, G., Kohlstedt, D.L., 1996. Water in the oceanic upper mantle: implications for rheology, melt extraction and the evolution of the lithosphere. Earth and Planetary Science Letters 144, 93–108. doi:10.1016/0012-821X(96)00154-9

Hui, H., Peslier, A.H., Rudnick, R.L., Simonetti, A., Neal, C.R., 2015. Plume-cratonic lithosphere interaction recorded by water and other trace elements in peridotite xenoliths from the Labait volcano, Tanzania: Water of Labait peridotite xenoliths. Geochemistry, Geophysics, Geosystems 16, 1687–1710. doi:10.1002/2015GC005779

Ingrin, J., Skogby, H., 2000. Hydrogen in nominally anhydrous upper-mantle minerals: concentration levels and implications. European Journal of Mineralogy 12, 543–570. doi:10.1127/ejm/12/3/0543

Ingrin, J., Blanchard, M. 2006. Diffusion of Hydrogen in Minerals. Reviews in Mineralogy and Geochemistry 62, 291–320. doi:10.2138/rmg.2006.62.13

Ingrin J., Azevedo-Vannson S., France L. 2019. Identification of two distinct OH infrared signatures in pyroxenes from pyroxenite xenoliths. Geophysical Research Abstracts, EGU General Assembly 2019; Vol. 21, EGU2019-8997

Karato, S., 1990. The role of hydrogen in the electrical conductivity of the upper mantle. Nature 347, 272–273.

Kendrick, M.A., Arculus, R.J., Danyushevsky, L.V., Kamenetsky, V.S., Woodhead, J.D., Honda, M., 2014. Subduction-related halogens (Cl, Br and I) and H_2O in magmatic glasses from Southwest Pacific Backarc Basins. Earth and Planetary Science Letters 400, 165–176. doi:10.1016/j.epsl.2014.05.021

Kendrick, M.A., Jackson, M.G., Hauri, E.H., Phillips, D., 2015. The halogen (F, Cl, Br, I) and H_2O systematics of Samoan lavas: Assimilated-seawater, EM2 and high-3He/4He components. Earth and Planetary Science Letters 410, 197–209. doi:10.1016/j.epsl.2014.11.026

Keppler, H., 2003. Water solubility in carbonatite melts. Am. Mineral. 88, 1822-1824. doi:10.2138/am-2003-11-1224

Kilgore M.L., Peslier, A.H., Brandon, A.D., Lamb, W.M., 2018. Water and Oxygen Fugacity in the Lithospheric Mantle Wedge beneath the Northern Canadian Cordillera (Alligator Lake). Geochemistry, Geophysics, Geosystems 19, 3844–3869. doi:10.1029/2018GC007700

Kilgore, M.L., Peslier, A.H., Brandon, A.D., Schaffer, L., Morris, R.V., Graff, T.G., Agresti,

D.G, O'Reilly, S.Y., Griffin, W.L., Pearson, G., Gangi, K., Shaulis, B.J., 2020. Metasomatic control of hydrogen contents in the layered cratonic mantle lithosphere sampled by Lac de Gras xenoliths in the central Slave craton, Canada. Geochimica et Cosmochimica Acta 286, 29-53. doi:10.1016/j.gca.2020.07.013

Klemme, S., Blundy, J.D., Wood, B.J., 2002. Experimental constraints on major and trace element partitioning during partial melting of eclogite. Geochimica et Cosmochimica Acta 66, 3109–3123. doi:10.1016/S0016-7037(02)00859-1

Koornneef, J.M., Nikogosian, I., Van Bergen, M.J., Vroon, P.Z., Davies, G.R., 2019. Ancient recycled lower crust in the mantle source of recent Italian magmatism. Nature Communications 10, 3237. doi:10.1038/s41467-019-11072-5

Kornprobst, J., 1969. Le massif ultramafique des Beni Bouchera (Rif interne, Maroc): Etude des péridotites de haute temperature et de haute pression et des pyroxenolites, à grenat ou sans grenat, qui leur sont associées. Contributions to Mineralogy and Petrology 23, 283–322. doi:10.1007/BF00371425

Kovács, I., Green, D.H., Rosenthal, A., Hermann, J., O'Neill, H.ST.C., Hibberson, W.O., Udvardi, B., 2012. An Experimental Study of Water in Nominally Anhydrous Minerals in the Upper Mantle near the Water-saturated Solidus. Journal of petrology 53, 2067-2093. doi:10.1093/petrology/egs044

Kovács, I., Hermann, J., O'Neill, H.St.C., Gerald, J.F., Sambridge, M., Horvath, G., 2008. Quantitative absorbance spectroscopy with unpolarized light: Part II. Experimental evaluation and development of a protocol for quantitative analysis of mineral IR spectra. American Mineralogist 93, 765–778. doi:10.2138/am.2008.2656

Lambart, S., Laporte, D., Schiano, P., 2009. An experimental study of pyroxenite partial melts at 1 and 1.5GPa: Implications for the major-element composition of Mid-Ocean Ridge Basalts. Earth and Planetary Science Letters 288, 335–347.

doi:10.1016/j.epsl.2009.09.038

Lambart, S., Laporte, D., Schiano, P., 2013. Markers of the pyroxenite contribution in the major-element compositions of oceanic basalts: Review of the experimental constraints, Lithos, 160–161, 14–36. doi:10.1016/j.lithos.2012.11.018

Lambart, S., Laporte, D., Provost, A., Schiano, P., 2012. Fate of Pyroxenite-derived Melts in the Peridotitic Mantle: Thermodynamic and Experimental Constraints. Journal of petrology 53, 451-476. doi:10.1093/petrology/egr068

Lambart, S., M. B. Baker, and E. M. Stolper, 2016. The role of pyroxenite in basalt genesis: Melt-PX, a melting parameterization for mantle pyroxenites between 0.9 and 5 GPa, Journal of Geophysical Research: Solid Earth 121. doi:10.1002/2015JB012762

Lee, D.-C., Halliday, A.N., Davies, G.R., Essene, E.J., Fitton, J.G., Temdjim, R., 1996. Melt Enrichment of Shallow Depleted Mantle: A Detailed Petrological, Trace Element and Isotopic Study of Mantle-Derived Xenoliths and Megacrysts from the Cameroon Line. Journal of Petrology 37, 415–441. doi:10.1093/petrology/37.2.415

Lenoir, X., Garrido, C.J., Bodinier, J.-L., Dautria, J.-M., 2000. Contrasting lithospheric mantle domains beneath the Massif Central (France) revealed by geochemistry of peridotite xenoliths. Earth and Planetary Science Letters 181, 359–375. doi:10.1016/S0012-821X(00)00216-8

Le Roux, V., Lee, C.-T.A., Turner, S.J., 2010. Zn/Fe systematics in mafic and ultramafic systems: Implications for detecting major element heterogeneities in the Earth's mantle. Geochimica et Cosmochimica Acta 74, 2779-2796. doi:10.1016/j.gca.2010.02.004

Li, P., Xia, Q.-K., Deloule, E., Chen, H., Gu, X.-Y., Feng, M., 2015. Temporal variation of H_2O content in the lithospheric mantle beneath the eastern North China Craton: Implications for the destruction of cratons. Gondwana Research 28, 276–287.

doi:10.1016/j.gr.2014.03.012

Li, H.-Y., Chen, R.-X., Zheng, Y.-F., Hu, Z., 2018. Water in garnet pyroxenite from the Sulu orogen: Implications for crust-mantle interaction in continental subduction zone. Chemical Geology 478, 18–38. doi:10.1016/j.chemgeo.2017.09.025

Libowitzky, E., Rossman, G.R., 1997. An IR absorption calibration for water in minerals. American Mineralogist 82, 1111–1115. doi:10.2138/am-1997-11-1208

Mallick, S., Standish, J.J, Bizimis, M., 2015. Constraints on the mantle mineralogy of an ultra-slow ridge: Hafnium isotopes in abyssal peridotites and basalts from the 9–25◦E Southwest Indian Ridge. Earth and Planetary Science Letters 410, 42-53. doi:10.1016/j.epsl.2014.10.048

Martin, L.H., Schmidt, M.W., Mattsson, H.B., Guenther, D., 2013. Element Partitioning between Immiscible Carbonatite and Silicate Melts for Dry and H2O-bearing Systems at 1–3 GPa. Journal of Petrology 54, 2301-2338. doi:10.1093/petrology/egt048

Marty, B., Avice, G., Sano, Y., Altwegg, K., Balsiger, H., Hässig, M., Morbidelli, A., Mousis, O., Rubin, M., 2016. Origins of volatile elements (H, C, N, noble gases) on Earth and Mars in light of recent results from the ROSETTA cometary mission. Earth and Planetary Science Letters 441, 91–102. doi:10.1016/j.epsl.2016.02.031

Matsyuk, S.S., Langer, K., Hösch, A., 1998. Hydroxyl defects in garnets from mantle xenoliths in kimberlites of the Siberian platform. Contributions to Mineralogy and Petrology 132, 163–179. doi:10.1007/s004100050414

McDonough, W.F., Sun S.S., 1995. The composition of the Earth. Chemical Geology 120, 223-253.

Michael, P.J., 1988. The concentration, behavior and storage of H_2O in the suboceanic upper mantle: Implications for mantle metasomatism. Geochimica et Cosmochimica Acta 52, 555-566. doi:10.1016/0016-7037(88)90110-X

Michael, P., 1995. Regionally distinctive sources of depleted MORB: Evidence from trace elements and H_2O. Earth and Planetary Science Letters 131, 301–320. doi:10.1016/0012-821X(95)00023-6

Montanini, A., Tribuzio, R., Thirlwall, M., 2012. Garnet clinopyroxenite layers from the mantle sequences of the Northern Apennine ophiolites (Italy): Evidence for recycling of crustal material. Earth and Planetary Science Letters 351-352, 171-181. doi:10.1016/j.epsl.2012.07.033

Morgan, J.P., Blackman, D.K., Sinton, J.M., 1992. Mantle Flow and Melt Generation at Mid-Ocean Ridges. Geophysical Monograph Series 71, 361

Njombie, M.P.W., Temdjim, R., Foley, S.F., 2018. Petrology of spinel lherzolite xenoliths from Youkou volcano, Adamawa Massif, Cameroon Volcanic Line: mineralogical and geochemical fingerprints of sub-rift mantle processes. Contributions to Mineralogy and Petrology 173. doi:10.1007/s00410-018-1438-5

Njome, A.S. and de Wit, M.J., 2014, The Cameroon Line: Analysis of an intraplate magmatic province transecting both oceanic and continental lithospheres: Constraints, controversies and models. Earth-Science Reviews, 139, 168-194.

Novella, D., Frost, D.J., Hauri, E.H., Bureau, H., Raepsaet, C., Roberge, M., 2014. The distribution of H_2O between silicate melt and nominally anhydrous peridotite and the onset of hydrous melting in the deep upper mantle. Earth and Planetary Science Letters 400, 1–13. doi:10.1016/j.epsl.2014.05.006

O'Hara, M.J., Yoder, H.S., 1967. Formation and fractionation of basic magmas at high pressures. Scottish Journal of Geology 3, 67-117. doi:10.1144/sjg03010067

O'Leary, J.A., Gaetani, G.A., Hauri, E.H., 2010. The effect of tetrahedral Al3+ on the partitioning of water between clinopyroxene and silicate melt. Earth and Planetary Science Letters 297, 111–120. doi:10.1016/j.epsl.2010.06.011

Pearson, D.G., Davies, G.R., Nixon, P.H., 1993. Geochemical Constraints on the Petrogenesis of Diamond Facies Pyroxenites from the Beni Bousera Peridotite Massif, North Morocco. Journal of Petrology 34, 125-172.

Patkó, L., Liptai, N., Kovács, I.J., Aradi, L.E., Xia, Q.-K., Ingrin, J., Mihály, J., O'Reilly, S.Y., Griffin, W.L., Wesztergom, V., Szabó, C., 2019. Extremely low structural hydroxyl contents in upper mantle xenoliths from the Nógrád-Gömör Volcanic Field (northern Pannonian Basin): Geodynamic implications and the role of post-eruptive re-equilibration. Chemical Geology 507, 23–41. doi:10.1016/j.chemgeo.2018.12.017

Perinelli, C., Armienti, P., Dallai, L., 2011. Thermal Evolution of the Lithosphere in a Rift Environment as Inferred from the Geochemistry of Mantle Cumulates, Northern Victoria Land, Antarctica. Journal of Petrology 52, 665-690. doi:10.1093/petrology/egq099

Peslier, A.H., Luhr, J.F., Post, J., 2002. Low water contents in pyroxenes from spinel-peridotites of the oxidized, sub-arc mantle wedge. Earth and Planetary Science Letters 201, 69–86. doi:10.1016/S0012-821X(02)00663-5

Peslier, A.H., 2010. A review of water contents of nominally anhydrous natural minerals in the mantles of Earth, Mars and the Moon. Journal of Volcanology and Geothermal Research 197, 239–258. doi:10.1016/j.jvolgeores.2009.10.006

Peslier, A.H., Woodland, A.B., Bell, D.R., Lazarov, M., Lapen, T.J., 2012. Metasomatic control of water contents in the Kaapvaal cratonic mantle. Geochimica et Cosmochimica Acta 97, 213–246. doi:10.1016/j.gca.2012.08.028

Peslier, A.H., Bizimis, M., 2015. Water in Hawaiian peridotite minerals: A case for a dry metasomatized oceanic mantle lithosphere: Water in Hawaii peridotites. Geochemistry, Geophysics, Geosystems 16, 1211–1232. doi:10.1002/2015GC005780

Peslier, A.H., Schönbächler, M., Busemann, H., Karato, S.-I., 2017. Water in the Earth's

Interior: Distribution and Origin. Space Science Reviews 212, 743–810. doi:10.1007/s11214-017-0387-z

Pezzali, I., France, L., Chazot, G., Vannucci, R., 2015. Analogues of exhumed pyroxenite layers in the Alboran domain sampled as xenoliths by Middle Atlas Cenozoic volcanism. Lithos. 230, 184–188. http://dx.doi.org/10.1016/j.lithos.2015.02.024

Rooney, T.O., Nelson, W.R., Dosso, L., Furman, T., Hanan, B., 2014. The role of continental lithosphere metasomes in the production of HIMU-like magmatism on the northeast African and Arabian plates. Geology 42, 419-422. doi:10.1130/G35216.1

Rossman, G.R., Smyth, J.R., 1990. Hydroxyl contents of accessory minerals in mantle eclogites and related rocks. American Mineralogist 75, 775–780.

Saal, A. E., Hart, S.R., Shimizu, N., Hauri, E.H., Layne, G.D., 1998. Pb Isotopic Variability in Melt Inclusions from Oceanic Island Basalts, Polynesia. Science. 282, 1481–1484.

Salters, V.J.M., Stracke, A., 2004. Composition of the depleted mantle. Geochemistry, Geophysics, Geosystems 5. doi:10.1029/2003GC000597

Sanfilippo, A., Tribuzio, R., Ottolini, L., Hamada, M., 2017. Water, lithium and trace element compositions of olivine from Lanzo South replacive mantle dunites (Western Alps): New constraints into melt migration processes at cold thermal regimes. Geochimica et Cosmochimica Acta 214, 51-72. doi:10.1016/j.gca.2017.07.034

Schaffer, L.A., Peslier, A.H., Brandon, A.D., Bizimis, M., Gibler, R., Norman, M., Harvey, J., 2019. Effects of melting, subduction-related metasomatism, and sub-solidus equilibration on the distribution of water contents in the mantle beneath the Rio Grande Rift. Geochimica et Cosmochimica Acta 266, 351-381. doi:10.1016/j.gca.2018.10.005

Selway, K., 2014. On the Causes of Electrical Conductivity Anomalies in Tectonically Stable Lithosphere. Surveys in Geophysics 35, 219–257. doi:10.1007/s10712-013-9235-1

Shorttle, O., Maclennan, J., Lambart, S., 2014. Quantifying lithological variability in the mantle. Earth and Planetary Science Letters 395, 24-40. doi:10.1016/j.epsl.2014.03.040

Skogby, H., 1994. OH incorporation in synthetic clinopyroxene. American Mineralogist, 79, 240-249

Sobolev, A.V., Hofmann, A.W., Kuzmin, D.V., Yaxley, G.M., Arndt, N.T., Chung, S.-L., Danyushevsky, L.V., Elliott, T., Frey, F.A., Garcia, M.O., Gurenko, A.A., Kamenetsky, V.S., Kerr, A.C., Krivolutskaya, N.A., Matvienkov, V.V., Nikogosian, I.K., Rocholl, A., Sigurdsson, I.A., Sushchevskaya, N.M., Teklay, M., 2007. The Amount of Recycled Crust in Sources of Mantle-Derived Melts. Science, 316, 412–417. doi:10.1126/science. 1138113

Sokol, A.G., Kupriyanov, I.N., Palyanov, Y.N., 2013. Partitioning of H_2O between olivine and carbonate–silicate melts at 6.3 GPa and 1400 °C: Implications for kimberlite formation. Earth and Planetary Science Letters 383, 58–67. doi:10.1016/j.epsl.2013.09.030

Stracke, A., Genske, F., Berndt, J., and Koornneef, J. M., 2019. Ubiquitous ultra-depleted domains in Earth's mantle. Nature Geoscience. 12, 851–855. doi:10.1038/s41561-019-0446-z

Suzuki, S., Nakashima, S., 2004. Grain Boundary Migration Kinetics of Quartz in the Presence of Water. Physicochemistry of Water in Geological and Biological Systems: Structures and Properties of Thin Aqueous Films, Universal Academy Press – Tokyo, Japan, 211–226.

Temdjim, R., Boivin, P., Chazot, G., Robin, C., Rouleau, É., 2004. L'hétérogénéité du manteau supérieur à l'aplomb du volcan de Nyos (Cameroun) révélée par les enclaves ultrabasiques. Comptes Rendus Geoscience 336, 1239–1244.

doi:10.1016/j.crte.2004.07.005

Tollan P, Hermann J, 2019. Arc magmas oxidised by water dissociation and hydrogen incorporation in orthopyroxene. Nat Geosci. 12, 667-671. doi:10.1038/s41561-019-0411-x

Touron, S., 2005. Empreintes géochimiques du métasomatisme mantellique sous le Massif Central, France. Thèse de l'Université Jean Monnet (Saint-Etienne, France)

Viljoen, K.S., Schulze, D.J., Quadling, A.G., 2005. Contrasting Group I and Group II Eclogite Xenolith Petrogenesis: Petrological, Trace Element and Isotopic Evidence from Eclogite, Garnet-Websterite and Alkremite Xenoliths in the Kaalvallei Kimberlite, South Africa. Journal of Petrology 46, 2059-2090. doi:10.1093/petrology/egi047

Wallace, P.J., 2002. Volatiles in Submarine Basaltic Glasses from the Northern Kerguelen Plateau (ODP Site 1140): Implications for Source Region Compositions, Magmatic Processes, and Plateau Subsidence. Journal of Petrology 43, 1311–1326. doi:10.1093/petrology/43.7.1311

Warren, J.M., Hauri, E.H., 2014. Pyroxenes as tracers of mantle water variations. Journal of Geophysical Research: Solid Earth 119, 1851–1881. doi:10.1002/2013JB010328

Weis, F.A., Ros, L., Reichart, P., Skogby, H., Kristiansson, P., Dollinger, G., 2018. Hydrogen concentration analysis in clinopyroxene using proton–proton scattering analysis. Physics and Chemistry of Minerals 45, 669–678. doi:10.1007/s00269-018-0953-2

Wittig, N., Baker, J.A., Downes, H., 2007. U–Th–Pb and Lu–Hf isotopic constraints on the evolution of sub-continental lithospheric mantle, French Massif Central. Geochimica et Cosmochimica Acta 71, 1290–1311. doi:10.1016/j.gca.2006.11.025

Workman, R.K., Hart, S.R., Jackson, M., Regelous, M., Farley, K.A., Blusztajn, J., Kurz, M., Staudigel, H., 2004. Recycled metasomatized lithosphere as the origin of the Enriched Mantle II (EM2) end-member: Evidence from the Samoan Volcanic Chain.

Geochemistry, Geophysics, Geosystems 5. doi:10.1029/2003GC000623

Workman, R.K., Hart, S.R., 2005. Major and trace element composition of the depleted MORB mantle (DMM). Earth and Planetary Science Letters 231, 53–72. doi:10.1016/j.epsl.2004.12.005

Workman, R.K., Hauri, E., Hart, S.R., Wang, J., Blusztajn, J., 2006. Volatile and trace elements in basaltic glasses from Samoa: Implications for water distribution in the mantle. Earth and Planetary Science Letters 241, 932–951. doi:10.1016/j.epsl.2005.10.028

Xia, Q.-K., Hao, Y., Li, P., Deloule, E., Coltorti, M., Dallai, L., Yang, X., Feng, M., 2010. Low water content of the Cenozoic lithospheric mantle beneath the eastern part of the North China Craton. Journal of Geophysical Research 115. doi:10.1029/2009JB006694

Xia, Q.-K., Liu, J., Liu, S.-C., Kovács, I., Feng, M., Dang, L., 2013. High water content in Mesozoic primitive basalts of the North China Craton and implications on the destruction of cratonic mantle lithosphere. Earth and Planetary Science Letters 361, 85–97. doi:10.1016/j.epsl.2012.11.024

Xia, Q.-K., Liu, J., Kovács, I., Hao, Y.-T., Li, P., Yang, X.-Z., Chen, H., Sheng, Y.-M., 2017. Water in the upper mantle and deep crust of eastern China: concentration, distribution and implications. National Science Review. doi:10.1093/nsr/nwx016

Yang, Y., Ingrin, J., Xia, Q, Liu, W., 2019. Nature of hydrogen defects in clinopyroxenes from room temperature up to 1000 °C: Implication for the preservation of hydrogen in the upper mantle and impact on electrical conductivity. Am. Mineral. 104, 79-93. doi:10.2138/am-2019-6661

Yang, S., Humayun, M., Salters, J.M., 2020. Elemental constraints on the amount of recycled crust in the generation of mid-oceanic ridge basalts (MORBs). Science Advances 6,

eaba2923. doi:10.1126/sciadv.aba2923

Yu, Y., Xu, X.-S., Griffin, W.L., O'Reilly, S.Y., Xia, Q.-K., 2011. H_2O contents and their modification in the Cenozoic subcontinental lithospheric mantle beneath the Cathaysia block, SE China. Lithos 126, 182–197. doi:10.1016/j.lithos.2011.07.009

Zhao, Y.H., Ginsberg, S.B., Kohlstedt, D.L., 2004. Solubility of hydrogen in olivine: dependence on temperature and iron content. Contributions to Mineralogy and Petrology,147, 155–161.

Fig. 1. The distribution of orthopyroxene, clinopyroxene, garnet, and whole-rock water contents (ppm) in peridotite (left) and pyroxenite (right). Data are from Peslier et al. (2002, 2012), Peslier (2010), Xia et al. (2010, 2013), Yu et al. (2011), Hao et al. (2012, 2014, 2016a, 2016b, 2018), Doucet et al. (2014), Warren and Hauri (2014), Bizimis and Peslier (2015), Demouchy et al. (2015), Li et al. (2015, 2018) and Peslier and Bizimis (2015), Kilgore et al. (2018, 2020), Schaffer et al. (2019), Ashley et al. (2020). Data of this study are in green. On average, pyroxenites are more water-rich than peridotites.

Fig. 2. Simplified geologic maps and sampling locations (red stars) in (a) the French Massif Central and (b) the Adan awa Volcanic Plateau (modified from France et al., 2015), black areas represent volcanic provinces. The stars indicate the samples location.

Fig. 3. (a, b) Photomicrographs and (c, d) X-ray elemental maps of the studied samples. (a) Sample LN78 showing garnets that often enclose green spinel (g-Spl) and contain numerous spinel (also brown spinel, b-Spl), plagioclase, orthopyroxene, and clinopyroxene inclusions surrounded by radial fractures. (b) A large grain of pyroxene with clinopyroxene and orthopyroxene exsolutions in sample LN78. (c) Millimetric granular assemblages in sample

YK03; thin garnet exsolutions are visible in clinopyroxenes. (d) Deformed clinopyroxene megacryst containing exsolutions of garnet and orthopyroxene in sample YK05.

Fig. 4. Sample-averaged unpolarized FTIR spectra of clinopyroxene, orthopyroxene, and garnet in samples from the FMC (LN78, LP27, SD53, Le Pouget) and AVP (YK03, YK05, YK12, YK13, YK16). Each average spectrum is normalized to 1-cm sample thickness and the reported water concentrations were calculated using the mineral-specific calibration of Bell et al. (1995) for clinopyroxenes and orthopyroxenes. The water concentrations in garnets are below the detection limit (<0.5 ppm). Clinopyroxene and orthopyroxene in FMC samples (LN78, LP27, SD53) are atypical ('type 2'), with the main water band occurring at lower wavenumbers (between 3515 and 3520 cm^{-1}) than in the other samples ('type 1'). The dashed lines at 3630 cm^{-1} and 3515 cm^{-1} highlight the main water bands in type-1 and type-2 spectra, respectively.

Fig. 5. Polarized FTIR spectra obtained of (a, b) clinopyroxene and (c) the average spectrum of garnets in sample YK01. Garnets are anhydrous (below the detection limit, <0.5 ppm). All spectra were normalized to 1-cm sample thickness. (a) Spectra over 3000–4000 cm^{-1}, with peaks corresponding to OH bands. (b) Spectra over 1200–2400 cm^{-1}, with peaks corresponding to lattice overtones specific to each orientation. $Cpx_1^{90°}/Cpx_1^{180°}$ and $Cpx_2^{90°}/Cpx_2^{180°}$ correspond to the orientations of the first and second thin sections, respectively.

Fig. 6. Comparison of the integrated absorptions of mineral cores and rims in (a) clinopyroxenes and (b) orthopyroxenes. Each point indicates the ratio of the integrated

absorption values measured at the rim and core of the same crystal. Most samples plot along on the 1:1 correlation line, highlighting the lack of core-rim zonation. This result indicates that the minerals did not experience diffusive re-equilibration, suggesting that there was no loss or gain of water during xenolith transport. The integrated absorption at the core and rim of each mineral are from profile measurements along the crystal; because the spectra are similar along the entire profiles, only the core and rim values are shown for clarity.

Fig. 7. (a) Clinopyroxene, (b) orthopyroxene, and (c) whole-rock (WR) water contents in FMC and AVP pyroxenites calculated using the calibration of Bell et al. (1995). The range shaded in blue indicates water contents of FMC peridotite xenoliths reported by Gu et al. (2018) and Denis et al. (2015). The low water concentrations of whole-rock peridotites are related to their low modal proportion of pyroxenes and high modal proportion of olivine, which contains relatively little water.

Fig. 8. Major element contents versus water concentrations in clinopyroxene and orthopyroxene in FMC and AVP pyroxenites. Mg# (= 100 × Mg/(Mg + Fe)) versus water content in (a) clinopyroxene and (c) orthopyroxene. (b) CaO versus water content in clinopyroxene. (d) Al_2O_3 versus water content in orthopyroxene. Dashed purple lines highlight linear relationships between major element contents and water concentrations in FMC pyroxenite minerals; any correlation is not obvious for the AVP samples. These results indicate that the water and major element contents of pyroxenites were acquired during a common equilibration (or re-equilibration) episode in the FMC, but during separate events in the AVP. Major element compositions are from France et al. (2015).

Fig. 9. Clinopyroxene vs. orthopyroxene water concentrations in peridotites from the

literature (Peslier et al., 2002, 2012; Peslier, 2010; Xia et al., 2010, 2013; Yu et al., 2011; Hao et al., 2012, 2014, 2016a, 2016b; Doucet et al., 2014; Warren and Hauri, 2014; Demouchy et al., 2015; Hui et al., 2015; Li et al., 2015; Peslier and Bizimis, 2015; Denis et al., 2018), pyroxenites from the literature (Warren and Hauri, 2014; Bizimis and Peslier, 2015, Hao et al., 2016a, 2018), and pyroxenites in this study (colored symbols). Red lines define the 1.5:1 and 3.5:1 partitioning of water between clinopyroxene and orthopyroxene; this equilibrium range encompasses the values of the pyroxenites studied herein, suggesting that the pyroxenes in these samples are in equilibrium with each other. Lines of $D_{H_2O}^{Cpx-Opx}$ = 1.5 and 3.5 are added for reference.

Fig. 10. Whole-rock Ti/Eu ratios as a function of whole-rock $(La/Sm)_N$ ratios (normalized to chondrites; Anders and Grevesse, 1989). The $(La/Sm)_N$ ratio is used here as a proxy of metasomatic overprinting. The Ti/Eu ratios of FMC pyroxenites are negatively correlated with $(La/Sm)_N$ ratios, suggesting a carbonatitic metasomatic overprint. See text for further details.

Fig. 11. (a) clinopyroxene (calculated using the calibration of Bell et al., 1995) and (b) whole-rock (WR) water concentrations (calculated from mineral-specific water contents and sample modal mineralogy) as a function of La/Sm_N. Both the clinopyroxene and whole-rock water contents are negatively correlated with $(La/Sm)_N$ for the FMC pyroxenites.

Fig. 12. (a) Clinopyroxene, (b) orthopyroxene, and (c) whole-rock (WR) water concentrations (ppm H_2O; calculated using the calibration of Bell et al., 1995) as a function of temperature (TNG09, °C; France et al., 2015). Correlations with R^2 = 0.95 and 0.99 are observed for FMC minerals and whole-rocks, whereas only the whole-rock water contents show good correlation

with temperature estimates in the AVP with $R^2 = 0.98$.

Fig. 13. Whole-rock water concentrations as a function of H_2O/Ce ratio for pyroxenites from the literature and the present study, with mantle reservoirs shown for comparison. Ce and water concentration values for the reservoirs (DMM, FOZO, HIMU, EM, and PM) are from Bizimis and Peslier (2015) and are presented as a reference frame for magmas worldwide. Types I and II pyroxenites are from Li et al. (2018), Hawaiian pyroxenites are from Bizimis and Peslier (2015), and Cr-, Al-, and Grt-pyroxenites are from Hao et al (2018). The most metasomatized samples from the literature (Hao et al., 2018; symbols outlined in black) are characterized by low H_2O/Ce ratios.

Fig. 14. Non-modal, incremental batch-melting models of representative FMC and AVP garnet pyroxenites presented on a [H_2O] (ppm) versus H_2O/Ce diagram. [H_2O] and H_2O/Ce strongly vary at low degrees of melting, and reach H_2O/Ce values similar to those of the starting pyroxenites after >10% partial melting.

Table 1: The distribution of orthopyroxene, clinopyroxene, garnet, and whole-rock water contents (ppm) in peridotite and pyroxenite as a function of geological origin.

Source	Minerals	Mean water content in peridotite (ppm)	Standard deviation	Mean water content in pyroxenite (ppm)	Standard deviation
Craton [b] [c] [d] [e] [f] [g] [h] [i] [j] [k] [l] [p] [q] [t]	Opx	116	94	56	49
	Cpx	240	185	146	94
	Grt	17	25	9	17
	WR	58	48	216	224
Off-craton [a] [c] [m] [s] [u]	Opx	146	69	143	171
	Cpx	347	143	363	180
	Grt	36	92	-	-
	WR	81	36	268	72
Oceanic lithosphere	Opx	125	97	201	49
	Cpx	290	111	425	78

[c] [n] [o] [r] [v]	Grt	-	-	23	5
	WR	38	36	333	65

[a] Peslier et al. (2002) [b] Peslier et al. (2012) [c] Peslier (2010) [d] Xia et al. (2010) [e] Xia et al. (2013) [f] Yu et al. (2011) [g] Hao et al. (2012) [h] Hao et al. (2014) [i] Hao et al. (2016a) [j] Hao et al. (2016b) [k] Hao et al. (2018) [l] Doucet et al. (2014) [m] Warren and Hauri (2014) [n] Bizimis and Peslier (2015) [o] Demouchy et al. (2015) [p] Li et al. (2015) [q] Li et al. (2018) [r] Peslier and Bizimis (2015) [s] Kilgore et al. (2018) [t] Kilgore et al. (2020) [u] Schaffer et al. (2019) [v] Ashley et aal. (2020)

Table 2. Modal compositions, equilibrium temperatures, and $(La/Sm)_N$ ratios.

Location	French Massif Central				Adamawa Volcanic Plateau					
Sample	LN78	LP27	SD53	Le Pouget	YK01	YK03	YK05	YK12	YK13	YK16
Thickness of sections (µm)	233-316	260-306	154-274	179-207	500-560	239-295	229-298	167-328	231-293	169-273
Modal composition										
Clinopyroxene (%)	40	70	55	61	60	45	60	45	65	70
Orthopyroxene (%)	22	5	10	3	0	15	17	40	17	0
Garnet (%)	30	15	20	33	30	26	23	10	8	28
Spinel (%)	8	10	5	3	10	14	0	5	10	2
Equilibrium temperature from major elements[b]										
T (°C)	1017	930	866	716		872	916	888	977	
$(La/Sm)_{N\ Cpx}$[b]	1.018	1.454	0.227	0.034	0.244	0.774	0.111	0.176	1.875	1.380
$(La/Sm)_{N\ WR}$[b]	1.771	1.880	0.808	0.037	0.248	0.728	0.327	0.181	1.771	1.536

[a] Although SD53 contains orthopyroxene, they are too altered and contain too many fluid inclusions for reliable analyses.

[b] Data from France et al. (2015).

Table 3. Water concentrations, H_2O/Ce ratios, and water partition coefficients.

Location	French Massif Central				Adamawa Volcanic Plateau					
Sample	LN78	LP27	SD53	Le Pouget	YK01	YK03	YK05	YK12	YK13	YK16
Integral absorption										
Cpx (cm^{-2})	264	554	849	1098	911	1106	1065	1118	1179	1619
Error (cm^{-2})	(+29;-16)	(+46;-86)	(+66;-102)	(+299;-158)	(+87;-136)	(+77;-130)	(+69;-55)	(+101;-124)	(+112;-142)	(+51;-250)
Number of cpx analyses per sample	29	31	30	24		29	23	30	28	34
Opx (cm^{-2})	301	383		515		765	711	614	731	
Error (cm^{-2})	(+74;-47)	(+39;-36)		(+22;-53)		(+97;-116)	(+20;-49)	(+21;-33)	(+92;-34)	
Number of opx analyses per sample	30	30		16		30	27	28	23	
Water concentration (Bell et al., 1995)										
Cpx [H_2O] (ppm)	112	234	359	465	386	468	451	473	499	685
Error (ppm)	(+25 ; -15)	(+45 ; -53)	(+66 ; -69)	(+185 ; -100)	(+78 ; -85)	(+82 ; -89)	(+77 ; -59)	(+94 ; -87)	(+102 ; -96)	(+92 ; -154)
Opx [H_2O] (ppm)	61	77		104		155	144	124	148	
Error (ppm)	(+22 ; -13)	(+15 ; -12)		(+14 ; -18)		(+35 ; -33)	(+17 ; -20)	(+15 ; -15)	(+33 ; -17)	
Water										

concentration (Libowitzky and Rossman, 1997)										
Cpx [H_2O] (ppm)	85	179	275	357	296	360	344	362	382	525
Error (ppm)	(+9 ; -5)	(+15 ; -28)	(+21 ; -33)	(+96 ; -52)	(+28 ; -44)	(+25 ; -43)	(+23 ; -17)	(+33 ; -40)	(+36 ; -46)	(+16 ; -81)
Opx [H_2O] (ppm)	78	100		135		201	185	160	191	
Error (ppm)	(+19 ; -12)	(+10 ; -10)		(+6 ; -14)		(+26 ; -30)	(+5 ; -13)	(+6 ; -8)	(+24 ; -9)	
Other data										
[H_2O] Whole rock (ppm)[a]	58	168	198	287	231	234	295	263	349	480
Error (ppm)	(+15 ; -9)	(+32 ; -38)	(+36 ; -38)	(+113 ; -61)	(+47 ; -51)	(+42 ; -45)	(+49 ; -39)	(+48 ; -45)	(+ 72 ; -66)	(+64 ; -108)
[H_2O] Whole rock (ppm)[b]	51	130	151	222	177	192	238	227	281	368
Error (ppm)	(+8 ; -5)	(+11 ; -20)	(+12 ; -18)	(+59 ; -32)	(+17 ; -26)	(+15 ; -24)	(+14 ; -13)	(+17 ; -22)	(+28 ; -31)	(+12 ; -57)
H_2O/Ce Whole rock[c]	30	44	166	2388	257	202	508	370	79	201
Error	(+8 ; -5)	(+8 ; -10)	(+31 ; -32)	(+945 ; -512)	(+52 ; -56)	(+36 ; -39)	(+84 ; -66)	(+68 ; -64)	(+16 ; -15)	(+27 ; -45)
$D^{Cpx/Melt}_{H2O}$[d]	0.019	0.019	0.018	0.016	0.017	0.015	0.015	0.015	0.017	0.017
Error	(+0.010 ; -0.006)	(+0.010 ; -0.007)	(+0.010 ; -0.006)	(+0.009 ; -0.006)	(+0.009 ; -0.006)	(+0.008 ; -0.005)	(+0.007 ; -0.005)	(+0.008 ; -0.005)	(+0.009 ; -0.006)	(+0.009 ; -0.006)
$D^{Opx/Melt}_{H2O}$[d]	0.015	0.015		0.009		0.010	0.010	0.010	0.010	
Error	(+0.00	(+0.00		(+0.00		(+0.00	(+0.00	(+0.00	(+0.00	

	6 ; -0.004)	6 ; -0.004)		3 ; -0.002)		3 ; -0.002)	3 ; -0.002)	3 ; -0.002)	3 ; -0.003)	

[a] Water concentrations calculated using the method of Bell et al. (1995) and modal composition.

[b] Water concentrations calculated using the method of Libowitzky and Rossman (1997) and modal composition.

[c] Data from France et al. (2015).

[d] Calculated following O'Leary et al. (2010) as $\ln D_{H_2O}^{(Cpx-Melt)} = -4.2(\pm0.2) + 6.5(\pm0.5)X_{Al^{IV}}^{Cpx} - 1.0(\pm0.2)X_{Ca}^{Cpx}$ and $\ln D_{H_2O}^{(Opx-Melt)} = -5.66(\pm0.11) + 8.4(\pm1.1)X_{Al^{VI}}^{Opx} + 10(\pm2)X_{Ca}^{Opx}$.

Declaration of interests

The authors declare that they have no known competing financial interests or personal relationships that could have appeared to influence the work reported in this paper.

The authors declare the following financial interests/personal relationships which may be considered as potential competing interests:

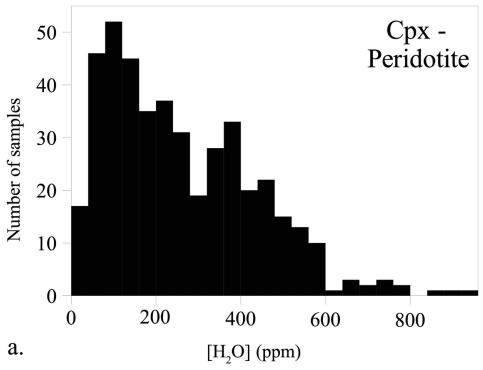

a.

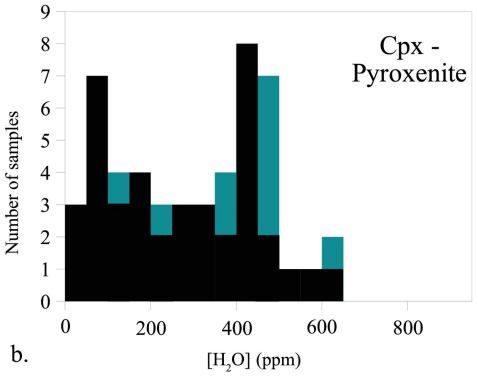

b.

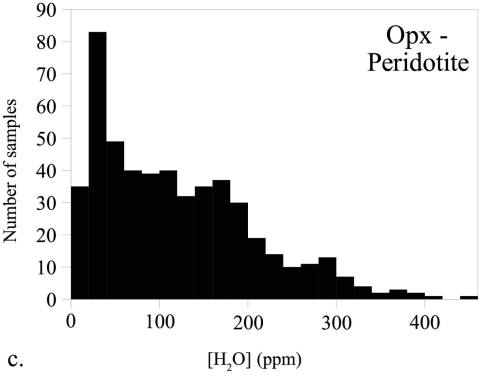

c.

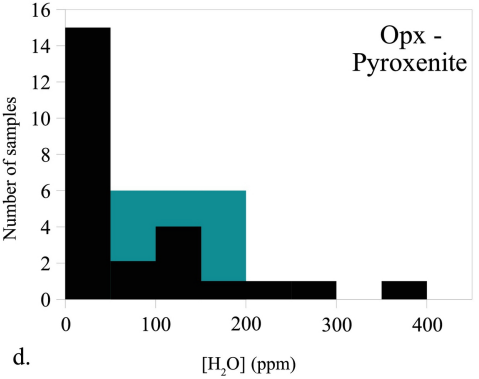

d.

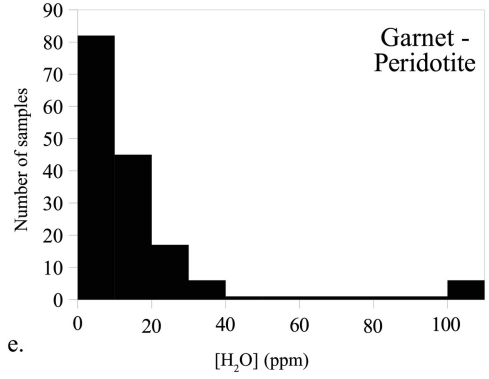

e.

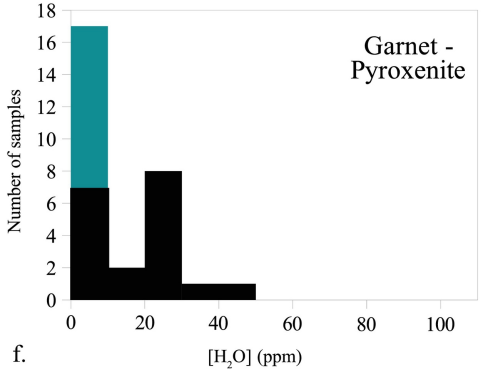

f.

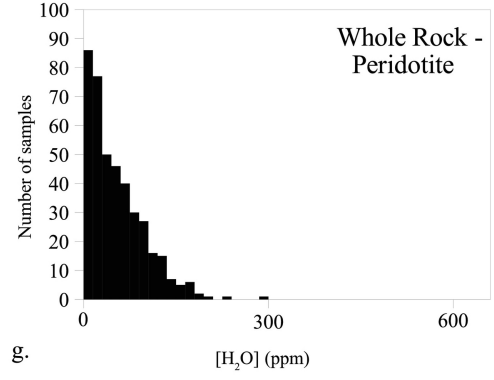

g.

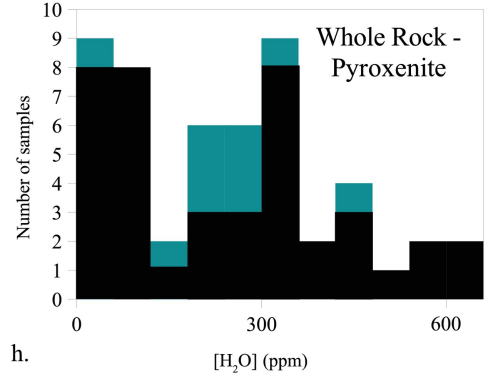

h.

Figure 1

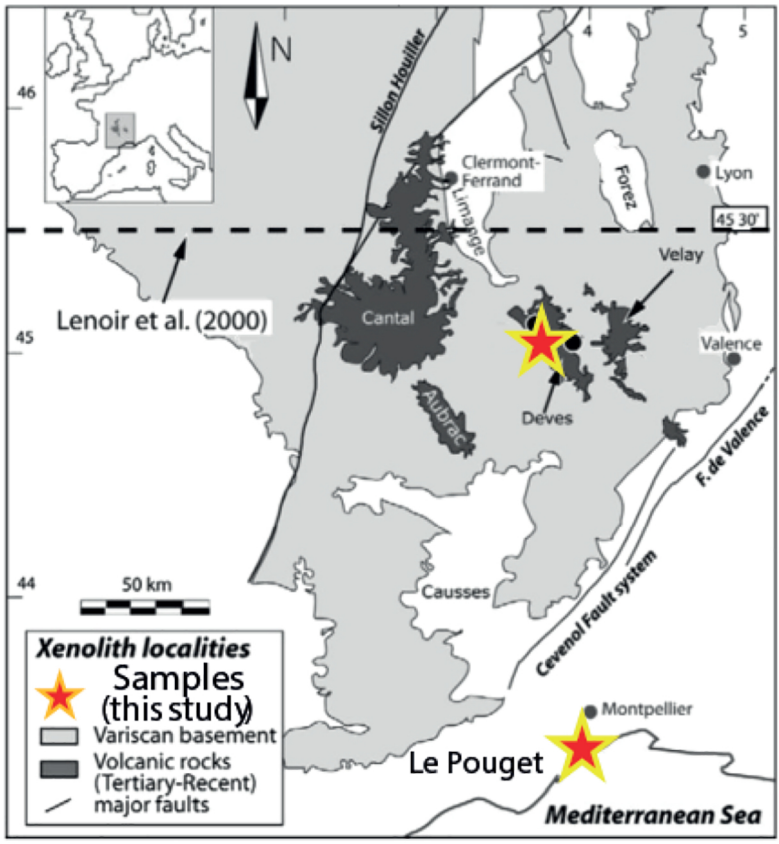
N
Sillon Houiller
Clermont-Ferrand
Lyon
Forez
Limagne
45 30'
Velay
Lenoir et al. (2000)
Cantal
Valence
Aubrac
Devès
F. de Valence
Causses
Cevenol Fault system
50 km
Xenolith localities
Samples (this study)
Variscan basement
Volcanic rocks (Tertiary-Recent)
major faults
Montpellier
Le Pouget
Mediterranean Sea
46
45
44
4
5

a.

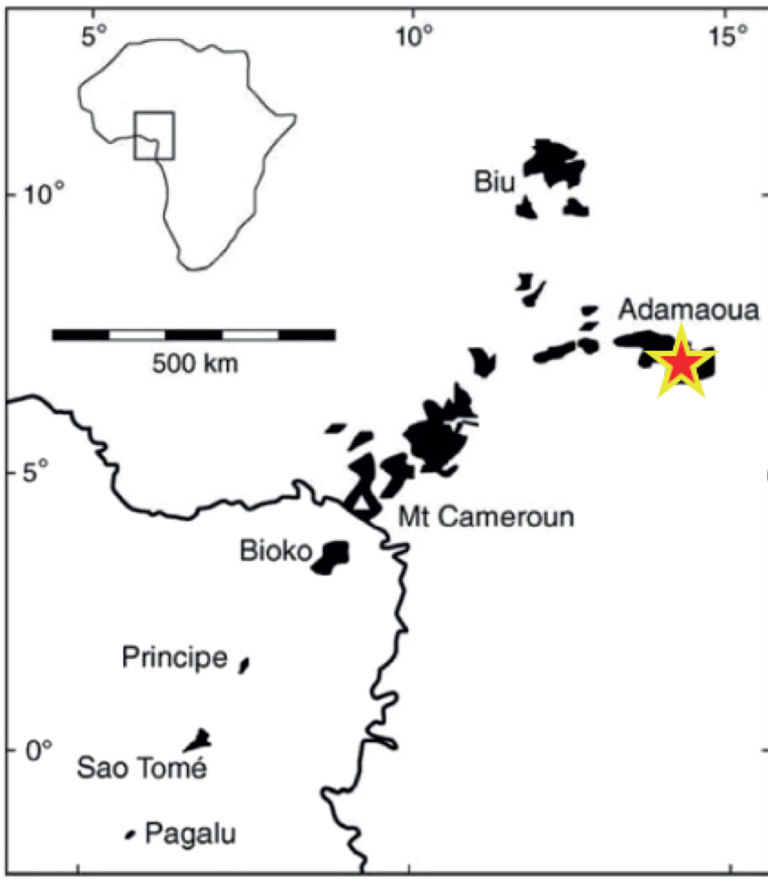
5°
10°
15°
10°
5°
0°
Biu
Adamaoua
500 km
Mt Cameroun
Bioko
Principe
Sao Tomé
Pagalu

b.

Figure 2

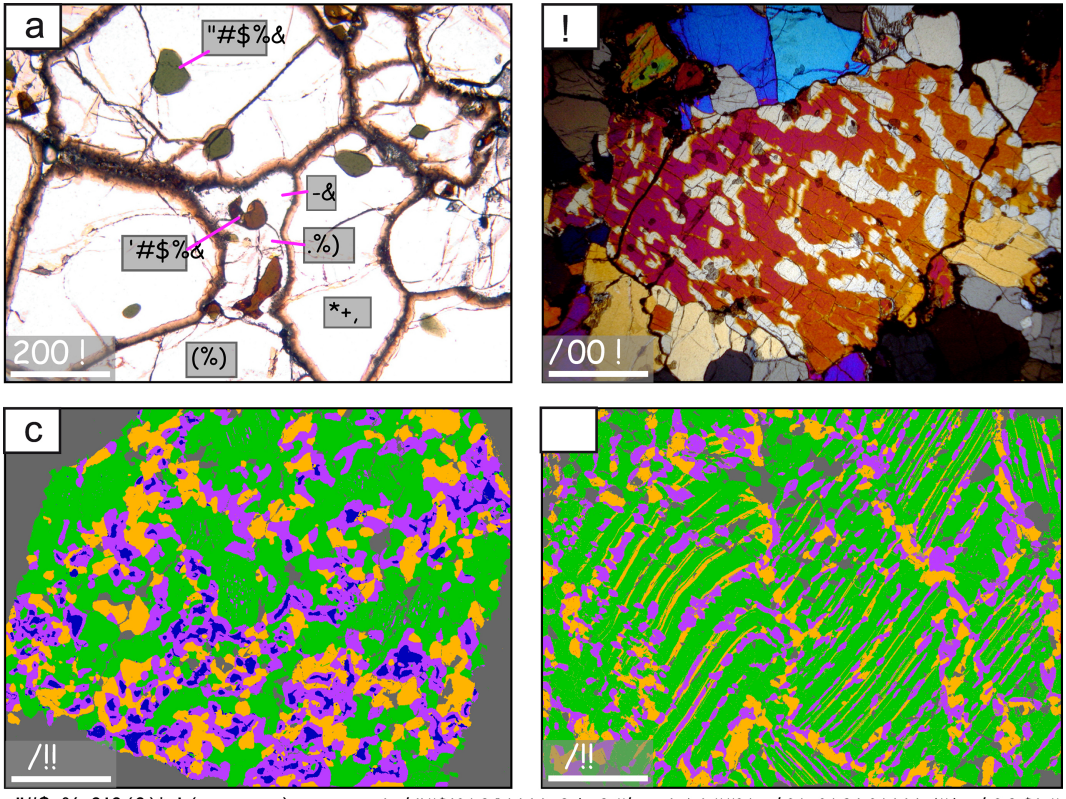

"#$a% &'&(&)*a' (a+ ,c a) -. gr ! / "#$!%&%(!) &*r&#/ g+r! ,) ' ##%- / %&,.%&'r%(!) /#* / 0&$! #

Figure 3

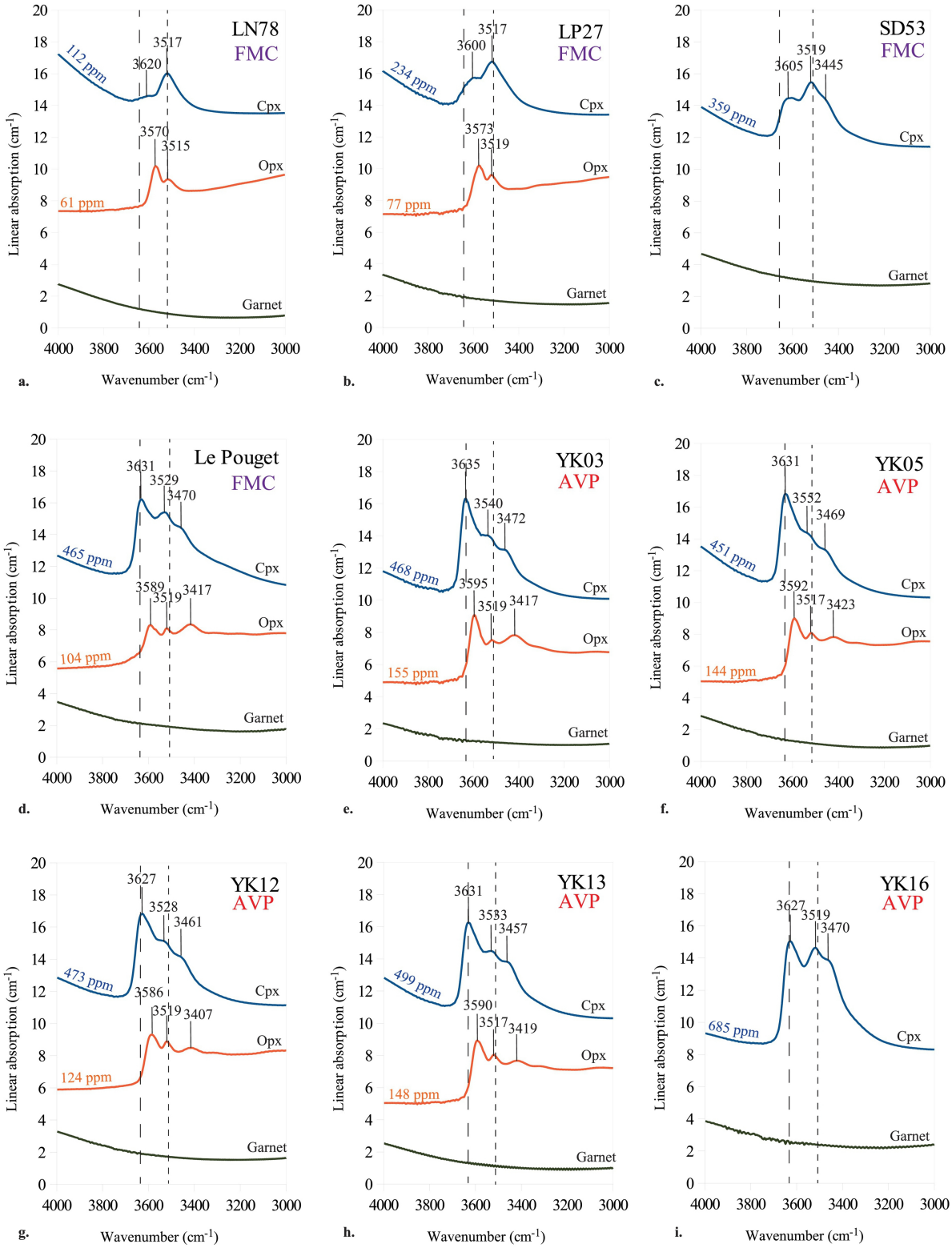
a.
LN78
FMC
112 ppm
3620
3517
Cpx
3570
3515
Opx
61 ppm
Garnet
b.
LP27
FMC
234 ppm
3600
3517
Cpx
3573
3519
Opx
77 ppm
Garnet
c.
SD53
FMC
359 ppm
3605
3519
3445
Cpx
Garnet
d.
Le Pouget
FMC
465 ppm
3631
3529
3470
Cpx
3589
3519
3417
Opx
104 ppm
Garnet
e.
YK03
AVP
468 ppm
3635
3540
3472
Cpx
3595
3519
3417
Opx
155 ppm
Garnet
f.
YK05
AVP
451 ppm
3631
3552
3469
Cpx
3592
3517
3423
Opx
144 ppm
Garnet
g.
YK12
AVP
473 ppm
3627
3528
3461
Cpx
3586
3519
3407
Opx
124 ppm
Garnet
h.
YK13
AVP
499 ppm
3631
3533
3457
Cpx
3590
3517
3419
Opx
148 ppm
Garnet
i.
YK16
AVP
685 ppm
3627
3519
3470
Cpx
Garnet
Linear absorption (cm-1)
Wavenumber (cm-1)

Figure 4

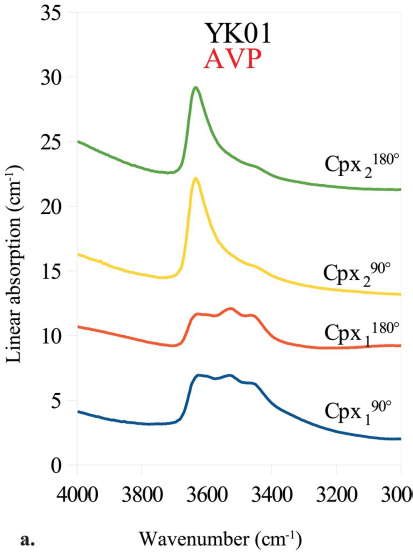
YK01
AVP
Cpx2180°
Cpx290°
Cpx1180°
Cpx190°
Linear absorption (cm-1)
Wavenumber (cm-1)

a.

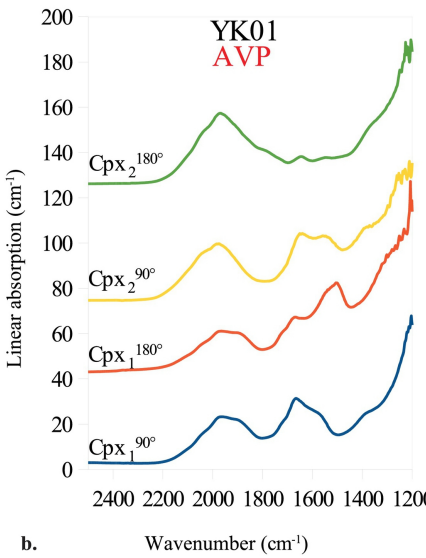
YK01
AVP
Cpx2180°
Cpx290°
Cpx1180°
Cpx190°
Linear absorption (cm-1)
Wavenumber (cm-1)

b.

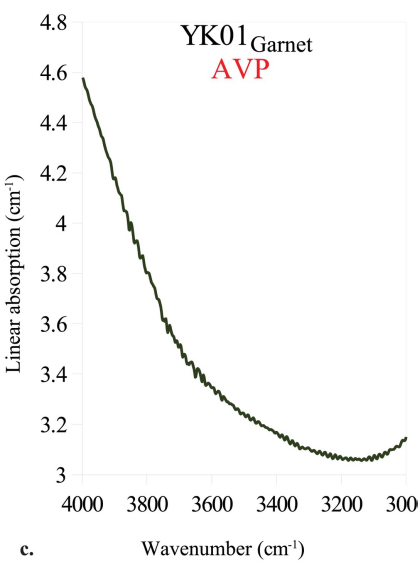
YK01Garnet
AVP
Linear absorption (cm-1)
Wavenumber (cm-1)

c.

Figure 5

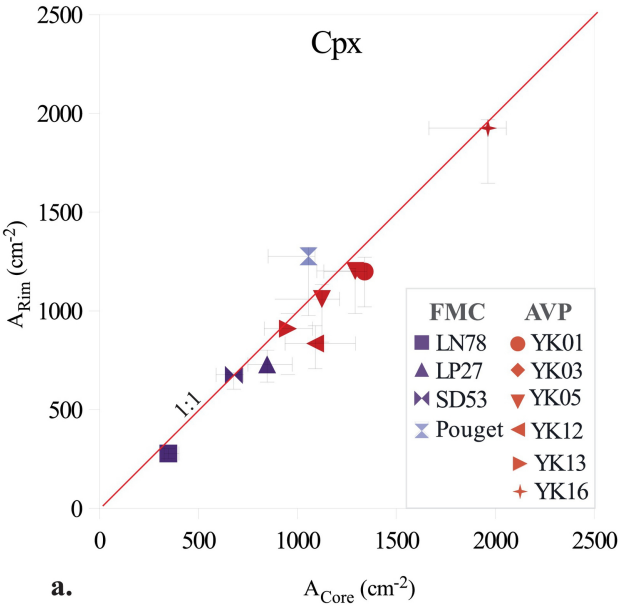
Cpx
2500
2000
1500
1000
500
0
0
500
1000
1500
2000
2500
A_Rim (cm-2)
A_Core (cm-2)
1:1
FMC
LN78
LP27
SD53
Pouget
AVP
YK01
YK03
YK05
YK12
YK13
YK16
a.

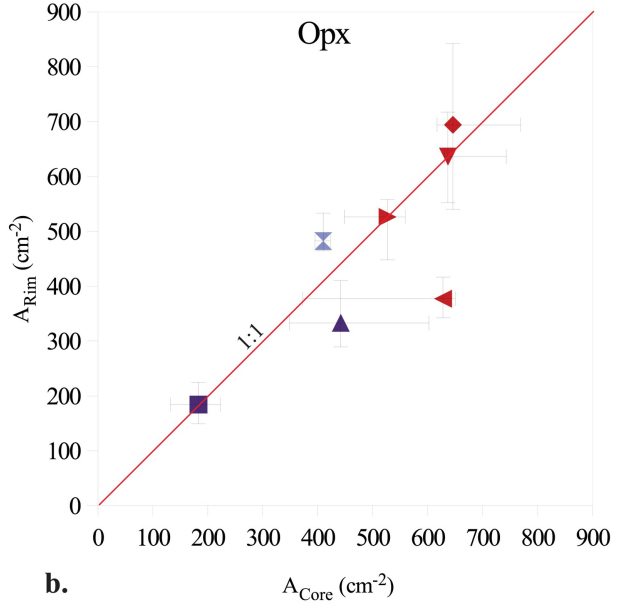
Opx
900
800
700
600
500
400
300
200
100
0
0
100
200
300
400
500
600
700
800
900
A_Rim (cm-2)
A_Core (cm-2)
1:1
b.

Figure 6

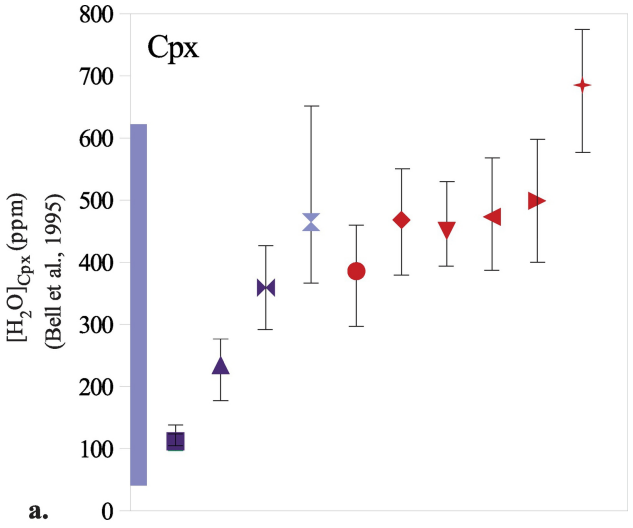
Cpx
$[H_2O]_{Cpx}$ (ppm)
(Bell et al., 1995)
800
700
600
500
400
300
200
100
0
a.

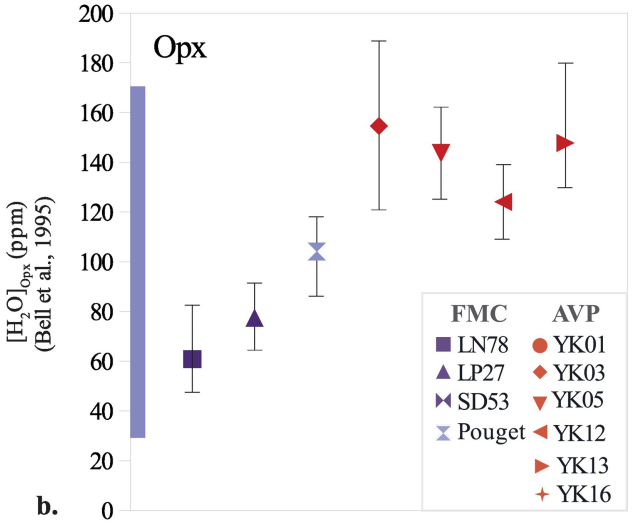
Opx
$[H_2O]_{Opx}$ (ppm)
(Bell et al., 1995)
200
180
160
140
120
100
80
60
40
20
0
b.
FMC
AVP
LN78
LP27
SD53
Pouget
YK01
YK03
YK05
YK12
YK13
YK16

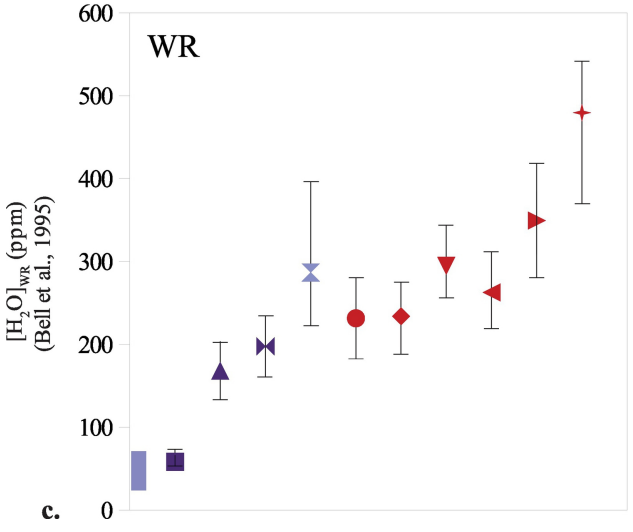
WR
$[H_2O]_{WR}$ (ppm)
(Bell et al., 1995)
600
500
400
300
200
100
0
c.

Figure 7

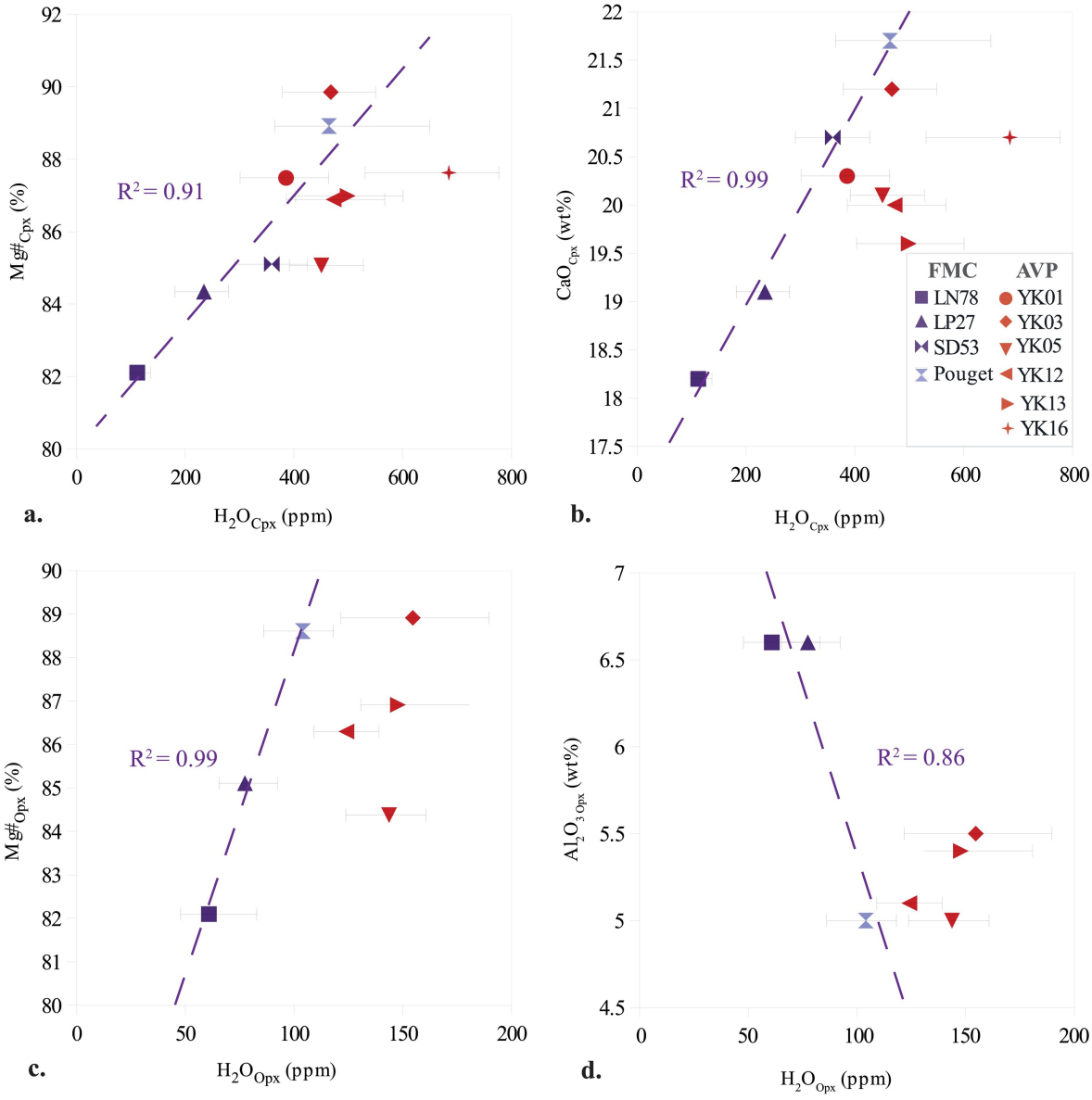
a.
$Mg^{\#}_{Cpx}$ (%)
H_2O_{Cpx} (ppm)
$R^2 = 0.91$
b.
CaO_{Cpx} (wt%)
H_2O_{Cpx} (ppm)
$R^2 = 0.99$
FMC
LN78
LP27
SD53
Pouget
AVP
YK01
YK03
YK05
YK12
YK13
YK16
c.
$Mg^{\#}_{Opx}$ (%)
H_2O_{Opx} (ppm)
$R^2 = 0.99$
d.
$Al_2O_{3\ Opx}$ (wt%)
H_2O_{Opx} (ppm)
$R^2 = 0.86$

Figure 8

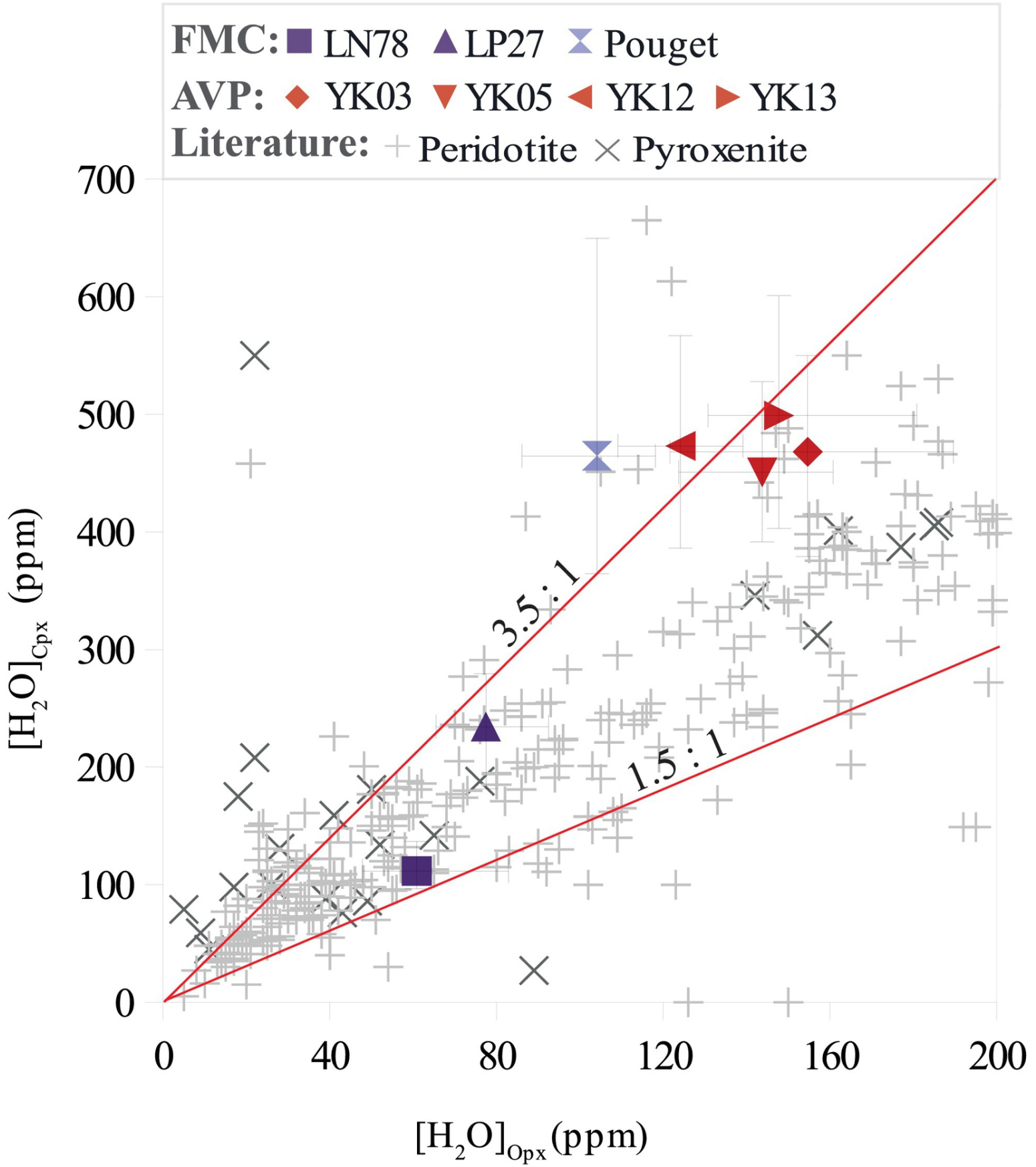
FMC: LN78 LP27 Pouget
AVP: YK03 YK05 YK12 YK13
Literature: Peridotite Pyroxenite
700
600
500
400
300
200
100
0
0
40
80
120
160
200
3.5 : 1
1.5 : 1
[H2O]Cpx (ppm)
[H2O]Opx (ppm)

Figure 9

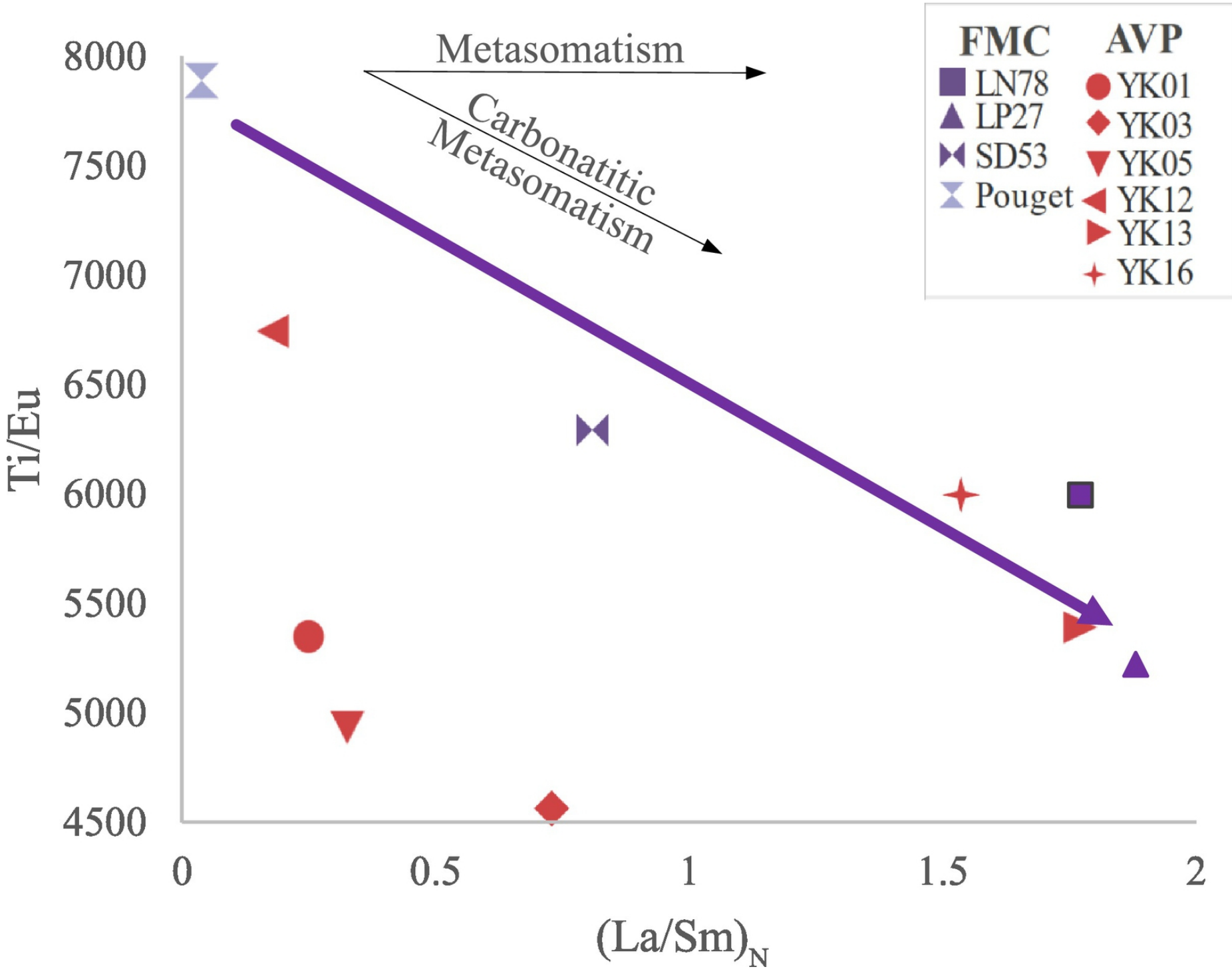
Metasomatism
Carbonatitic Metasomatism
FMC
LN78
LP27
SD53
Pouget
AVP
YK01
YK03
YK05
YK12
YK13
YK16
8000
7500
7000
6500
6000
5500
5000
4500
Ti/Eu
0
0.5
1
1.5
2
(La/Sm)N

Figure 10

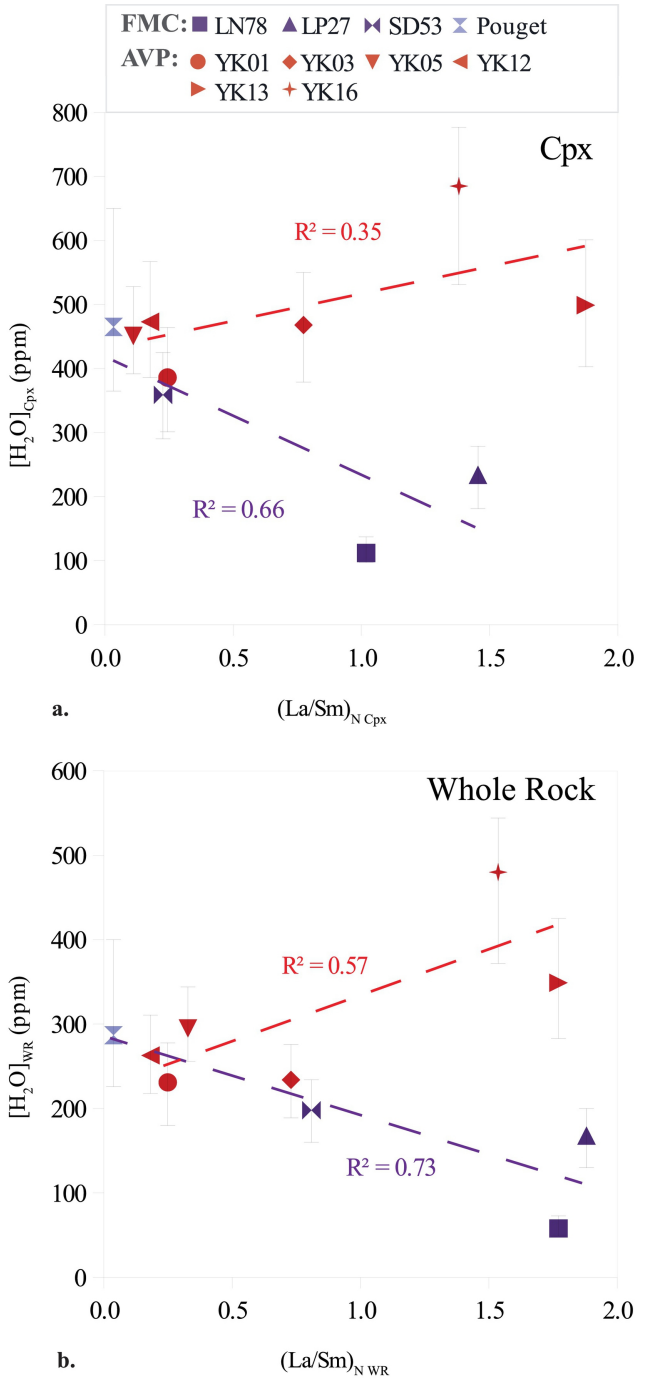
FMC: LN78 LP27 SD53 Pouget
AVP: YK01 YK03 YK05 YK12 YK13 YK16
Cpx
R² = 0.35
R² = 0.66
[H2O]Cpx (ppm)
(La/Sm)N Cpx
a.
Whole Rock
R² = 0.57
R² = 0.73
[H2O]WR (ppm)
(La/Sm)N WR
b.

Figure 11

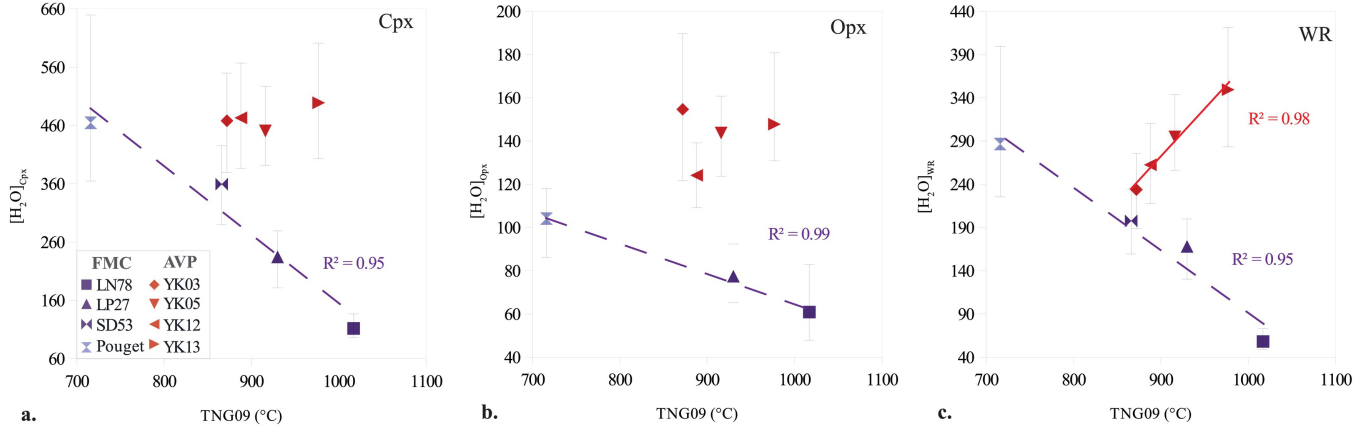
Cpx
[H2O]cpx
660
560
460
360
260
160
60
700
800
900
1000
1100
TNG09 (°C)
FMC
AVP
LN78
LP27
SD53
Pouget
YK03
YK05
YK12
YK13
R² = 0.95
a.
Opx
[H2O]opx
200
180
160
140
120
100
80
60
40
R² = 0.99
b.
WR
[H2O]WR
440
390
340
290
240
190
140
90
40
R² = 0.98
R² = 0.95
c.

Figure 12

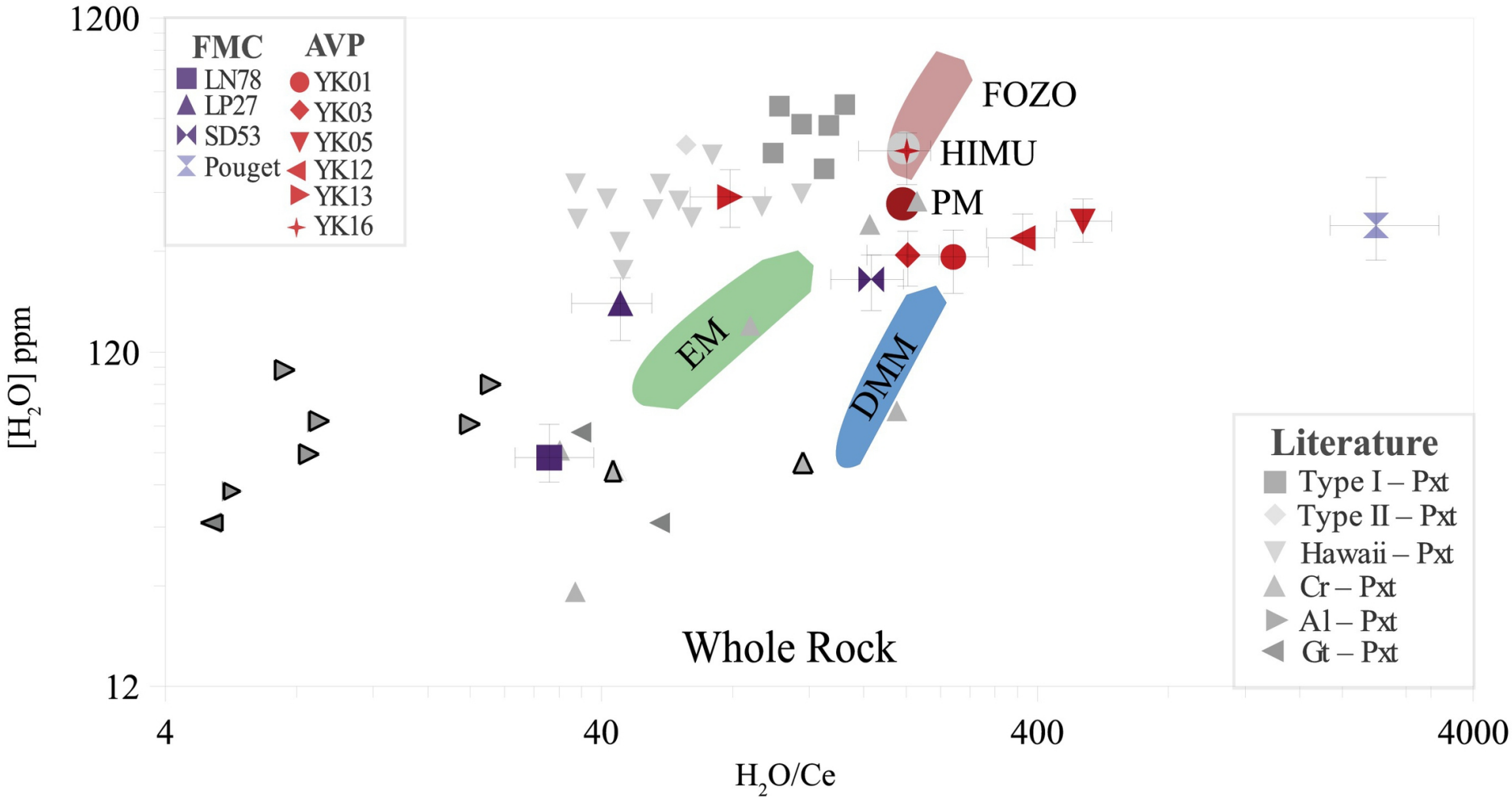
1200
120
12
[H2O] ppm
4
40
400
4000
H2O/Ce
FMC
LN78
LP27
SD53
Pouget
AVP
YK01
YK03
YK05
YK12
YK13
YK16
FOZO
HIMU
PM
EM
DMM
Whole Rock
Literature
Type I – Pxt
Type II – Pxt
Hawaii – Pxt
Cr – Pxt
Al – Pxt
Gt – Pxt

Figure 13

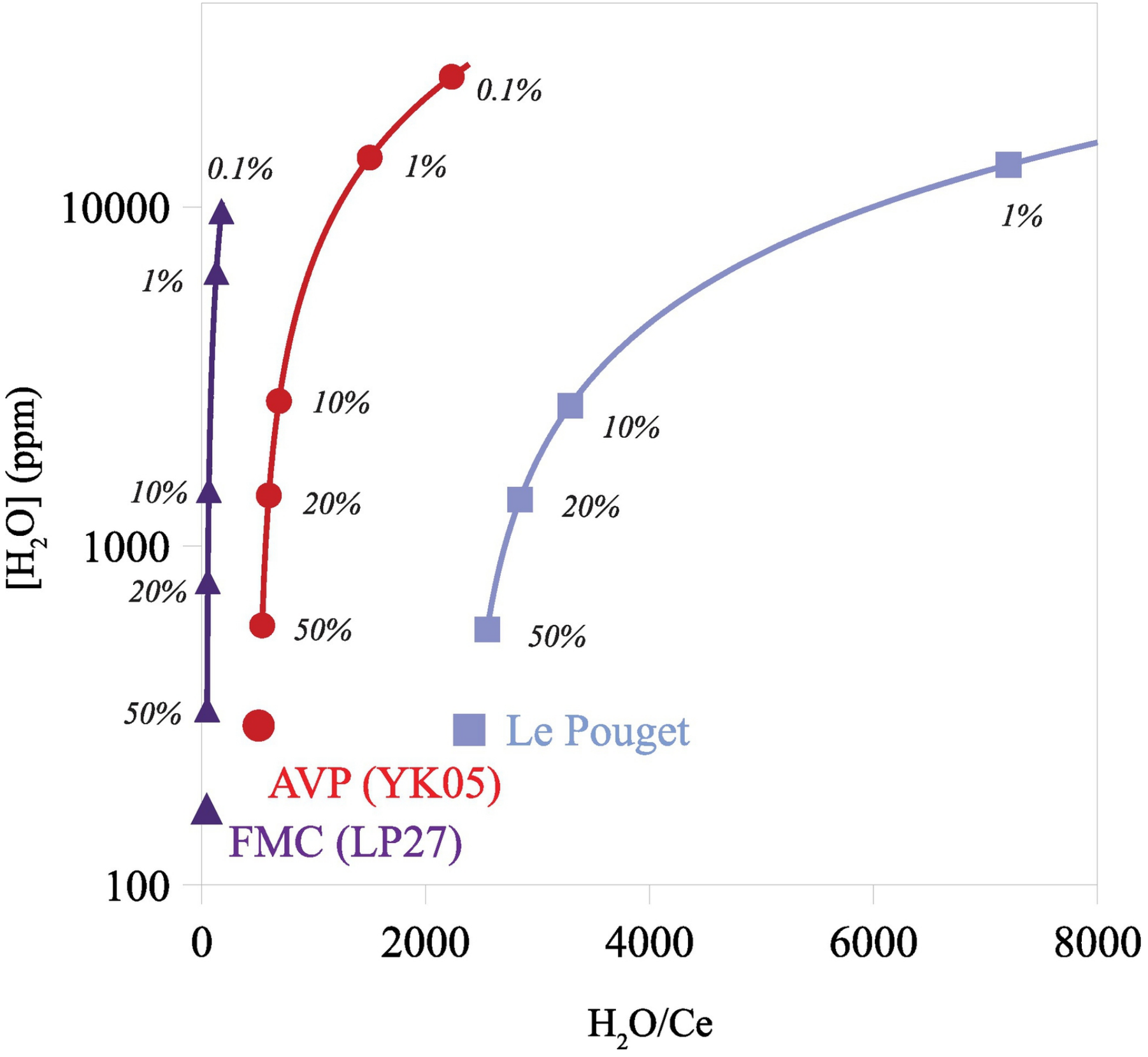
0.1%
1%
10%
20%
50%
0.1%
1%
10%
20%
50%
1%
10%
20%
50%
10000
1000
100
[H2O] (ppm)
0
2000
4000
6000
8000
H2O/Ce
Le Pouget
AVP (YK05)
FMC (LP27)

Figure 14